Accepted Article

Upper ocean distribution of glacial meltwater in the Amundsen Sea, Antarctica

Louise C. Biddle[1,3], Brice Loose[2], and Karen J. Heywood[3]

[1]Department of Marine Science, University of Gothenburg, Sweden
[2]Graduate School of Oceanography, University of Rhode Island, US
[3]Centre for Ocean and Atmospheric Sciences, School of Environmental Sciences, University of East Anglia, UK

Key Points:

- Oxygen isotope and noble gas data identify freshwater in the upper ocean across the Amundsen Sea
- Hydrographic calculations of meltwater are improved using noble gases as ground-truth
- We identify a new meltwater export pathway in the eastern channel in the Amundsen Sea

This article has been accepted for publication and undergone full peer review but has not been through the copyediting, typesetting, pagination and proofreading process which may lead to differences between this version and the Version of Record. Please cite this article as doi: 10.1029/2019JC015133

Corresponding author: Louise Biddle, louise.biddle@marine.gu.se

©2018 American Geophysical Union. All rights reserved.

Accepted Article

Abstract

Pine Island Ice Shelf, in the Amundsen Sea, is losing mass due to increased heat transport by warm ocean water penetrating beneath the ice shelf and causing basal melt. Tracing this warm deep water and the resulting glacial meltwater can identify changes in melt rate and the regions most affected by the increased input of this freshwater. Here, optimum multi-parameter analysis is used to deduce glacial meltwater fractions from independent water mass characteristics (standard hydrographic observations, noble gases and oxygen isotopes), collected during a ship-based campaign in the eastern Amundsen Sea in February-March 2014. Noble gases (neon, argon, krypton and xenon) and oxygen isotopes are used to trace the glacial melt and meteoric water found in seawater and we demonstrate how their signatures can be used to rectify the hydrographic trace of glacial meltwater, which provides a much higher resolution picture. The presence of glacial meltwater is shown to mask the Winter Water properties, resulting in differences between the water mass analyses of up to 4 g kg^{-1} glacial meltwater content. This discrepancy can be accounted for by redefining the "pure" Winter Water endpoint in the hydrographic glacial meltwater calculation. The corrected glacial meltwater content values show a persistent signature between 150 - 400 m of the water column across all of the sample locations (up to 535 km from Pine Island Ice Shelf), with increased concentration towards the west along the coastline. It also shows, for the first time, the signature of glacial meltwater flowing off-shelf in the eastern channel.

Plain Language Summary

Pine Island Ice Shelf in the Amundsen Sea, Antarctica, is melting due to warm ocean waters. The glacial meltwater that is produced is less salty and carries essential food for biological organisms, so where the glacial meltwater goes once it leaves the front of the ice-shelf is important to understand: less salt in the ocean at the surface makes it easier to form sea ice, and increased productivity from biological organisms can help draw carbon down into the ocean from the atmosphere. We use noble gases to identify where this glacial meltwater is, as the signature that the meltwater leaves in the gases is unique like a fingerprint. We use the noble gas meltwater signature to improve our identification of glacial meltwater using temperature, salinity and dissolved oxygen (hydrographic observations), which are easier and cheaper to collect so cover a larger area. Using the improved signature from hydrographic observations we identify the presence of glacial meltwater between 150-400 m depth everywhere across the continental shelf. We also show, for the first time, glacial meltwater from the ice-shelf flowing off-shelf in the easternmost channel. These results are important as they show where glacial meltwater is affecting the ocean column most.

1 Introduction

The addition of glacial meltwater (GMW) to the ocean results in cooling and freshening of the water masses that it mixes with. In the seas surrounding Antarctica, studies have shown increasing volumes of GMW entering the water column, associated with calving of icebergs and basal melt from ice shelves (Pritchard et al., 2012; Shepherd et al., 2018). This fresher, colder water mass has been linked to freshening of Antarctic Bottom Water (AABW) in the Ross Sea (Jacobs & Giulivi, 2010; Schmidtko et al., 2014), and implicated in changes in sea ice extent and thickness surrounding the continent (Bintanja et al., 2013). In regions with more in-situ observations and focused modeling studies, such as the Amundsen Sea (Heywood et al., 2016), GMW has been shown to play an important role in modulating the strength of local circulation (Jourdain et al., 2017; Silvano et al., 2018; Webber et al., 2017). The presence of GMW affects the stratification and mixing of the upper ocean, resulting in changes in ocean-atmosphere heat and carbon exchange, altering biological and chemical properties of the mixed layer (Biddle et al.,

©2018 American Geophysical Union. All rights reserved.

Accepted Article

2017; Kim et al., 2016; Randall-Goodwin et al., 2015; St-Laurent et al., 2017). The potential impacts of GMW on the ocean, and linkages to the climate system, make it important to understand where this water mass is most frequently found, and understand its spatial (horizontal and vertical) and temporal variability.

The Amundsen Sea contains several ice shelves fed by the West Antarctic Ice Sheet, with Pine Island Ice Shelf (PIIS), Thwaites Ice Shelf and Getz Ice Shelves among these (Figure 1). This is also a location where warm modified Circumpolar Deep Water (mCDW) accesses the continental shelf through glacially carved channels, in particular through the eastern and central channels (Walker et al., 2007). The warm mCDW flows towards the grounding line of the ice shelves, resulting in higher basal melting rates (Jacobs et al., 1996; Payne et al., 2004; Jacobs et al., 2011), and linked to subsequent unstable retreat. Since the 1990s, multiple field campaigns have taken place in this region, operated by the British, US, Swedish, German, Korean research communities (Jacobs et al., 2012; Nakayama et al., 2013; Heywood et al., 2016; Kim et al., 2016). Within these studies, focus has been placed on identifying the mechanisms for the warm water to access the continental shelf and ice shelf (Walker et al., 2007; Thoma et al., 2008; Arneborg et al., 2012; Assmann et al., 2013; Wåhlin et al., 2013; Mallett et al., 2018), and identification of GMW has mainly occurred directly in front of the ice shelves, with the exception of three more recent studies (Nakayama et al., 2013; Kim et al., 2016; Biddle et al., 2017). This location bias is mainly due to the reliability associated with the tracers used to identify GMW, as it was unknown how reliable conservative tracers (and pseudo-conservative tracers such as dissolved oxygen concentration) would be with increasing distance from the ice shelves (Jenkins, 1999).

Recent work has shown that up to 500 km from PIIS, hydrographic tracers (conservative temperature, absolute salinity and dissolved oxygen concentrations) identify possible GMW signatures (Biddle et al., 2017). However, these conservative tracers are affected by atmospheric exchange in the mixed layer, and deeper in the water column by other water masses mixing in with the GMW. This will result in a loss of the meltwater signature. Noble gases are used as a reliable indicator of GMW, as the lighter noble gases (helium, He; neon, Ne; and argon, Ar) are highly oversaturated when the ice melts into the ocean water, and there are no other processes known to create this signature in the ocean (Hohmann et al., 2002; Loose & Jenkins, 2014; Beaird et al., 2015). The heavier noble gases, krypton (Kr) and xenon (Xe), are undersaturated in GMW, and so are used as additional 'fingerprints' to identify the GMW (Loose & Jenkins, 2014). The signature of GMW from noble gases has some variability associated with physical effects (such as air content in the ice), but this is relatively small compared to the variability and atmospheric effects seen with the hydrographic tracers. Previous studies have successfully used noble gases to identify GMW (Nakayama et al., 2013; Loose & Jenkins, 2014; Beaird et al., 2015; Kim et al., 2016; Huhn et al., 2018), but noble gas samples are both money- and time-expensive to collect and analyse. Oxygen isotope ratios are used in conjunction with absolute salinity to distinguish ocean water from meteoric water (GMW or local precipitation) or sea ice melt (Weiss et al., 1979; Jenkins, 1999; Randall-Goodwin et al., 2015). Together, these measurements distinguish GMW from surface input freshwater (from precipitation or sea ice melt).

In this study, we present hydrographic, noble gas and oxygen isotope data collected from the Amundsen Sea as part of the 2014 iSTAR research cruise (Section 2). We calculate freshwater distribution from oxygen isotope ratios (Section 3) and the distribution of glacial meltwater using noble gases (Section 4). The hydrographic GMW calculations are compared with the noble gases and improved using the noble gas GMW content as ground-truth, revealing a higher spatial resolution and more extensive dataset of GMW content (Section 5). Finally, we combine the GMW content with current velocity data to identify meltwater pathways across the eastern Amundsen Sea (Section 6).

©2018 American Geophysical Union. All rights reserved.

Accepted Article

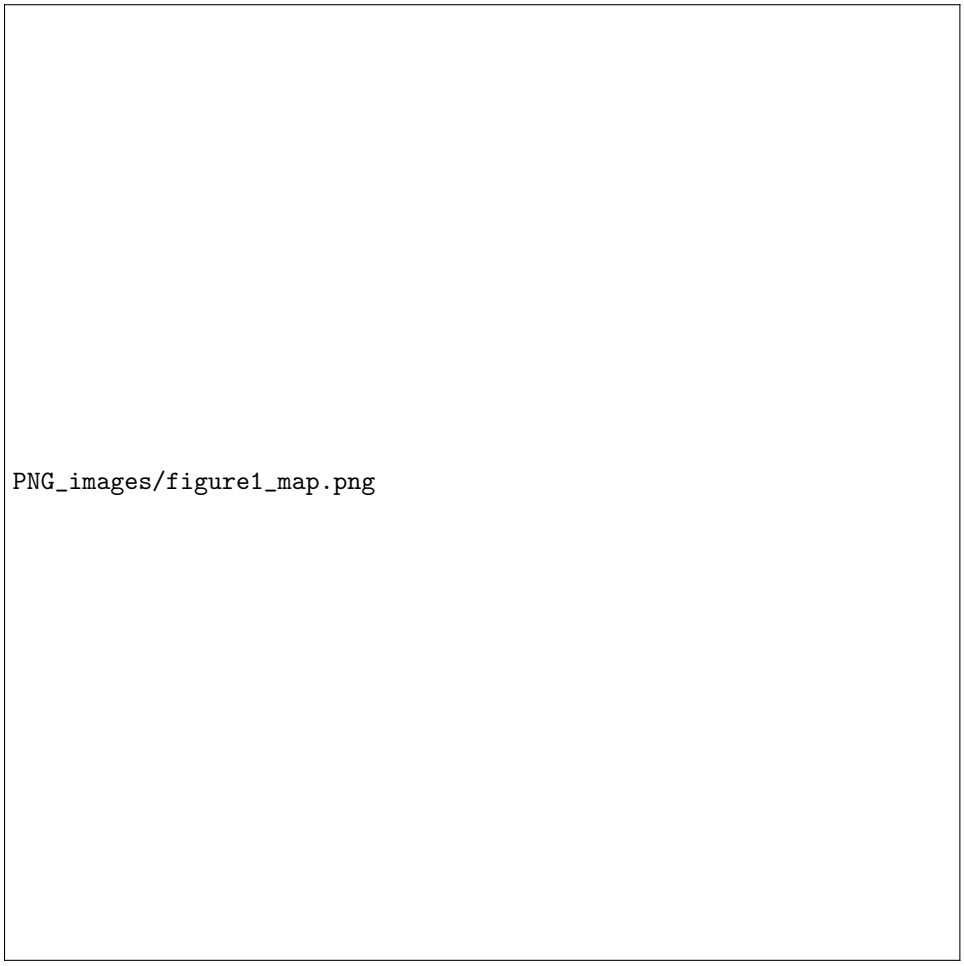

Figure 1. Map showing location of sample region in Antarctica (red box in inset), and enlarged map showing the CTD-only stations (pink dots), oxygen isotope and CTD only stations (blue squares) and all tracer stations (yellow triangle). Sections of interest are highlighted in black; A: central channel, B: eastern channel, C: south of Burke Island and D: ice shelf section. Bathymetry shown in the background, and local ice shelves are labelled: AIS, Abbott Ice Shelf; CIS, Cosgrove Ice Shelf; PIIS, Pine Island Ice Shelf; TIS, Thwaites Ice Shelf; Cr, Crosson Ice Shelf; DIS, Dotson Ice Shelf; GIS, Getz Ice Shelf.

2 Observations

The analysis included in this paper was conducted using data and water samples collected during the iSTAR Ocean2ice 2014 research cruise (Heywood et al., 2016) to the Amundsen Sea in the West Antarctic (Figure 1). In total, 105 Conductivity-Temperature-Depth (CTD) stations were occupied across the continental shelf, also measuring dissolved oxygen (using SBE911 with a SBE43 dissolved oxygen sensor). Temperature and salinity values are reported as conservative temperature (Θ) and absolute salinity (S_A), following TEOS-10 (IOC et al., 2010). The conservative temperature was calibrated using a deep SBE sensor, and dissolved oxygen values were calibrated using Winkler titrations of water samples.

In Θ, S_A and dissolved oxygen concentration ($c(O_2)$) space (Figure 2), the water masses encountered in 2014 are described in detail by Biddle et al. (2017). The mCDW

©2018 American Geophysical Union. All rights reserved.

Accepted Article

is found as the warmest, most saline and least oxygenated water mass on shelf, whilst the Winter Water (WW) is cooler, fresher and more oxygenated through interaction with the atmosphere (Table 1; Figure 2a). The GMW appears as a warmer, more saline and less oxygenated water mass than the WW due to its admixture with mCDW, but as a pure water mass GMW is cold, fresh and highly oxygenated (Table 1). All water mass content is reported as g kg^{-1}, which is comparable to ‰. Four sections are focused on in this paper (Sections A-D, Figure 1), and the Θ, S_A and $c(O_2)$ sections for these can be found in Heywood et al. (2016), Biddle et al. (2017) and as Figure S1 (Section B).

Water samples for oxygen isotope analysis were taken at 53 stations, and for noble gas (helium, neon, argon, krypton and xenon) analysis at 31 stations (Figure 1, Figures S2-5), with the two techniques coinciding at 19 stations. Noble gas samples (of 45 ml) were collected in copper tubes, which were sealed by crimping at both ends (Loose et al., 2016). The samples were analysed in the Isotope Geochemistry Facility at Woods Hole Oceanographic Institution. Samples are opened at both ends by compressing the chamber along the bellows. Subsequent to opening the samples, dissolved gas is quantitatively extracted from the water and captured inside an aluminosilicate glass bulb that is maintained at -196 °C using a liquid nitrogen bath. After gas extraction, the bulbs are attached to a dual mass spectrometric system and analyzed for He, Ne, Ar, Kr, and Xe (Stanley et al., 2009). The noble gases are isolated on two cryogenic traps and selectively warmed to sequentially release each gas into the Hiden Quadrupole Mass Spectrometer (QMS) for measurement by peak height manometry (Lott, 2001). The reproducibility from N = 6 duplicate samples was 1.8% for He, 1.6% for Ne, 0.5% for Ar, 0.1% for Kr and 0.3% for Xe. Analytical precision is 0.5% or better for Ar, Kr, and Xe and approximately 1% for He and Ne (Stanley et al., 2009). All gases are reported as μmol kg^{-1}. Helium concentrations are not reported in this study, due to local influence from mantle sources (Loose et al., 2018).

The water samples for oxygen isotope ratios ($\delta^{18}O$) were collected in 100 ml glass bottles and sealed further with Parafilm. Samples were transported by dark cool stow to the Natural Environment Research Council Isotope Geosciences Laboratory (NIGL) at the British Geological Survey. Water samples were analysed for $\delta^{18}O$ using an Isoprime mass spectrometer. Isotopic ratios are given as ‰ deviations from VSMOW2, and analytical reproducibility was <0.04 ‰ on duplicates.

We use current velocity data from a RDI 300kHz Workhorse Lowered Acoustic Doppler Current Profiler unit fitted to the CTD rosette frame. We are using LADCP velocity profiles that are co-located with the CTD stations and tracers collected.

3 Freshwater distribution

The freshwater sources in the Amundsen Sea consist of precipitation, glacial meltwater and sea ice melt (and sea ice growth as a sink). These sources are identified by the use of oxygen isotope ratios, where precipitation and glacial meltwater are grouped together as Meteoric Water Input (MWI), as they both form through snowfall. By using measured absolute salinity and oxygen isotope ratios, mCDW, MWI and Sea Ice Melt (SIM) are calculated and the distribution of freshwater in the Amundsen Sea observed.

3.1 Calculation of freshwater from oxygen isotopes

To calculate the fractions of mCDW and the two freshwater sources, the oxygen isotope ratios, $\delta^{18}O$, are used in combination with the absolute salinity (S_A) observations, following previous studies (Meredith et al., 2008; Price et al., 2008; Randall-Goodwin

©2018 American Geophysical Union. All rights reserved.

Accepted Article

Table 1. Endpoints used for the water masses in the Amundsen Sea.

	Θ	S_A	$c(O_2)$	$c(Ne)$ $\times10^{-3}$	$c(Ar)$	$c(Kr)$ $\times10^{-3}$	$c(Xe)$ $\times10^{-3}$	δ^{18}O
	(°C)	(g kg^{-1})	———	(μmol kg^{-1})	———			(‰)
mCDW	1.15	34.87	187	8.12	16.42	4.01	0.604	0.05
WW	-1.76	34.27	291	–	–	–	–	–
pWW	-1.80	34.32	295	–	–	–	–	–
AEW	–	–	–	8.43	17.52	4.32	0.660	–
GMW	-90.8	0	1125	91.6	44.46	5.84	0.414	–
MWI	–	0	–	–	–	–	–	-25
SIM	–	7	–	–	–	–	–	2.1

et al., 2015)(Equation 1),

$$\begin{pmatrix} \delta^{18}O_{mCDW} & \delta^{18}O_{SIM} & \delta^{18}O_{MWI} \\ S_{\mathrm{A},mCDW} & S_{\mathrm{A},SIM} & S_{\mathrm{A},MWI} \\ 1 & 1 & 1 \end{pmatrix} \begin{pmatrix} \mathrm{F_{mCDW}} \\ \mathrm{F_{SIM}} \\ \mathrm{F_{MWI}} \end{pmatrix} = \begin{pmatrix} \delta^{18}O_{obs} \\ S_{\mathrm{A},obs} \\ 1 \end{pmatrix}, \qquad (1)$$

where $\delta^{18}O_{mCDW}$ represents the oxygen isotope ratio endpoint for mCDW, F is the water mass fraction, and $\delta^{18}O_{obs}$ is the observed oxygen isotope ratio.

The mCDW that is present on the eastern Amundsen Sea shelf has a δ^{18}O of 0.05 ‰ and absolute salinity of 34.87 g kg^{-1} (Biddle et al., 2017) (Figure 3a; Table 1). Sea ice forms from seawater, which will have an oxygen isotope ratio close to VSMOW2 (δ^{18}O = 0 ‰), but during sea ice formation, the oxygen isotopes experience slight fractionation, with the sea ice preferably forming with the heavier oxygen isotopes (Price et al., 2008). This gives the resulting SIM a slight positive shift from seawater δ^{18}O with an endpoint of 2.1 ‰ and due to slight brine inclusions an absolute salinity of 7 g kg^{-1} (Randall-Goodwin et al., 2015) (Table 1). MWI around Antarctica has a very low (large negative) oxygen isotope ratio due to the loss of ^{18}O through precipitation north of the continent and therefore the ratio of ^{18}O to ^{16}O decreases. Typical values from the Antarctic Ice Sheet are between -20 ‰ and -40 ‰ (Meredith et al., 2008; Price et al., 2008). Here, we use a δ^{18}O of -25 ‰ and salinity of 0 g kg^{-1} to define MWI, following a recent study in the same region by Randall-Goodwin et al. (2015) (Table 1).

We use Monte Carlo simulations to estimate the uncertainties in the water mass calculation. Each endpoint is perturbed around the reported endpoint (Table 1) by the uncertainty associated with each tracer (environmental and measurement uncertainty). We run 10,000 simulations with end-point values randomly chosen within these prescribed bounds. The uncertainty is then represented by the standard deviation of the difference between the simulated runs and the unperturbed run. We find that the uncertainty associated with the MWI water mass fractions is 0.5 %, or 5 g kg^{-1}. This ± 5 g kg^{-1} variation in MWI content is anti-correlated with the SIM content whilst mCDW content remains stable.

3.2 Freshwater distribution in the Amundsen Sea

Using these calculations, we assess the water masses in the Amundsen Sea, and describe the vertical and spatial distribution of the different sources of freshwater. In vertical profile, both SIM and MWI have maximum concentrations at the surface (36.5 g kg^{-1} and 33.6 g kg^{-1} respectively), and MWI then decreases with depth (Figure 3b). The MWI content is most significant above 400 m, where the mean MWI content is 18 g kg^{-1}, correlating with the depth at which GMW is observed to flow out from beneath the ice shelf (Biddle et al., 2017; Garabato et al., 2017). Negative values of SIM indicate

©2018 American Geophysical Union. All rights reserved.

Accepted Article

net sea ice formation. Whilst the surface (< 40 m) shows SIM, below 60 m shows a net effect of sea ice growth, with values reaching -8.7 g kg^{-1}. This sea ice growth component decreases with depth to negligible sea ice contributions at depths below 600 m. As the measurements were taken at the end of the austral summer, the high surface SIM content reflects the result of the seasonal heating of the upper ocean, and also the strong stratification this produces, shown by the restriction of this signal to the top 40 m. The net sea ice growth throughout the rest of the water column is consistent with previous studies on the Amundsen Sea continental shelf (Randall-Goodwin et al., 2015), where significant sea ice export results in higher sea ice growth rates than sea ice melt rates (Stammerjohn et al., 2015).

These freshwater distributions are assessed spatially by calculating column inventories. To do this, profiles with 4 or more samples (excludes three stations) are linearly interpolated vertically, and MWI or SIM content is integrated over the top 500 m (Figure 3c,d). Out of 50 stations, 36 have negative column integrated SIM (indicating net sea ice growth), with mean SIM of -1.4 m. The stations south of Burke Island show net sea ice growth (27 out of 30), whilst half of those at the continental shelf edge show net SIM (Figure 3c). This agrees with previous studies that have suggested that the region between 70° S to 72° S, which spans the continental shelf edge, is characterised by sea ice drift (Stammerjohn et al., 2015). This indicates that sea ice will be brought into this area by drift and then melts in location over the summer resulting in net SIM. Closer to the coast, katabatic winds blow off the ice shelves, allowing sea ice export and net sea ice growth (Stammerjohn et al., 2015). There are two locations where the SIM signatures do not follow this pattern: a positive SIM signature in the centre of the Pine Island Trough and a negative SIM signature at the western edge of the eastern channel at the continental shelf edge.

Over all of the stations in the Amundsen Sea, the average MWI content is 7.5 m with a small standard deviation (1.8 m). This relatively small standard deviation is likely due to the combination of GMW and precipitation in the MWI content, as the Amundsen Sea is a region of relatively high precipitation (Lenaerts et al., 2012). The MWI content is greatest closest to PIIS and around Thwaites Ice Shelf, with values up to 10.7 m (Figure 3d). The mean MWI content for all stations south of Burke Island (Figure 3d) is 8.5 m, although they all have MWI content >6.1 m, with the exception of the most eastern station in the meridional section south of Burke Island (5 m). The mean column inventory of 9.5 m at the western end of the section is similar to values reported by Randall-Goodwin et al. (2015) 2° further west in 2010-11. The lowest column inventories are found in the off-shelf stations (<3.8 m), whilst the stations at the continental shelf edge have a mean MWI content of 6.4 m. The central channel shows lower MWI content than the eastern channel (6.2 m compared with 6.7 m). The stations that show negative SIM values at the western edge of the eastern channel also display higher MWI content of up to 8.6 m.

4 Distribution of glacial meltwater using noble gases

As the oxygen isotope ratios cannot be used to distinguish glacial meltwater from local precipitation, we use other tracers measured during the fieldwork. By using a similar method to the one used for oxygen isotope ratios, we identify different water masses in the Amundsen Sea using noble gas concentrations.

4.1 Calculation of water mass fractions

As there are more noble gas tracer constraints (plus mass conservation) than there are water masses to be identified, we use Optimum Multiparameter Analysis (OMPA) to calculate the water mass fractions (Loose & Jenkins, 2014; Biddle et al., 2017). This method is identical to the one used for hydrographic tracers (Θ, S_A, $c(O_2)$) by Biddle

©2018 American Geophysical Union. All rights reserved.

Accepted Article

et al. (2017). OMPA uses a least squares regression with a non-negativity constraint to solve the over-determined equation

$$\begin{pmatrix} \chi_{1,mCDW} & \chi_{1,AEW} & \chi_{1,GMW} \\ \chi_{2,mCDW} & \chi_{2,AEW} & \chi_{2,GMW} \\ \vdots & \vdots & \vdots \\ \chi_{n,mCDW} & \chi_{n,AEW} & \chi_{n,GMW} \\ 1 & 1 & 1 \end{pmatrix} \begin{pmatrix} \mathrm{F_{mCDW}} \\ \mathrm{F_{AEW}} \\ \mathrm{F_{GMW}} \end{pmatrix} = \begin{pmatrix} \chi_{1,obs} \\ \chi_{2,obs} \\ \vdots \\ \chi_{n,obs} \\ 1 \end{pmatrix}, \quad (2)$$

where $\chi_{n,k}$ is the noble gas tracer n of water mass k and $\mathrm{F_k}$ is the water mass fraction. The data are normalised and weighted, to account for variations between properties in measurement or environmental accuracy (in observations and/or endpoint determination). This approach is discussed further by Biddle et al. (2017).

The reliability of these water mass calculations is estimated using Monte Carlo analysis, where the endpoints used are varied by up to the largest uncertainty associated with each tracer. We find that the noble gas GMW concentrations are reliable to $\pm$ 0.5 g kg^{-1}, compared with $\pm$ 1 g kg^{-1} found for the hydrographic tracers (Biddle et al., 2017).

The water masses used in these calculations for the noble gases consist of mCDW, Air Equilibrated Water (AEW) and GMW. The atmospherically influenced water mass (AEW) represents surface saturation values of the noble gases (Loose & Jenkins, 2014), which differs slightly from the definition for WW used for identification with Θ, S_A and $c(O_2)$ (Table 1, Section 5), due to the limitations associated with defining an atmospheric endpoint in temperature and salinity. Temperature, salinity and dissolved oxygen are excluded from these OMPA calculations in order to provide two independent estimates of the GMW content.

The noble gases are useful for identifying GMW, as the sources and sinks of these gases are well known and they are not affected by biological or chemical processes within the water column. We use neon, argon, krypton and xenon to identify GMW (Figure 4). Neon has low solubility, and so is oversaturated in GMW, with values of 91.6 $\times 10^{-3}$ μmol kg^{-1} typical for Antarctic ice shelves (Loose et al., 2009), whilst argon acts similarly to dissolved oxygen, and is slightly oversaturated in GMW (44.46 μmol kg^{-1}; Table 1; Figure 4). The heavier noble gases, krypton and xenon are both undersaturated in GMW (Table 1; Figure 4). The other two water masses defined by noble gas characteristics are AEW and mCDW. As the concentration of noble gases in the atmosphere is known, we are able to use AEW as an endpoint, using surface values to represent the interaction of the atmosphere with the ocean (Table 1; Figure 4). Due to the few sources of noble gases in the deep ocean, the noble gas concentrations in mCDW are well established (Table 1).

4.2 Glacial meltwater signature from noble gases

We see similar GMW distributions from noble gases (NG GMW) through the water column and across the Amundsen Sea to those previously calculated from hydrographic observations by Biddle et al. (2017) (Figures 4e,f). The noble gases show the increased presence of GMW above the draft of the ice shelf at approximately 600 m and surface values directly in front of PIIS are up to 18 g kg^{-1}. Unlike the MWI content deduced from the oxygen isotopes, NG GMW values decrease at the surface for all CTD stations further than 100 km from PIIS. This is an artefact due to interaction of the upper ocean with the atmosphere eradicating the noble gas signatures in the surface layer, visible as the inverse correlation between the low surface NG GMW values and high AEW content (Figure 4e). Of particular interest though is the presence of GMW across all CTD stations between 50 - 400 m depth (Figure 4e), which differs from previous studies that reported negligible GMW content at the continental shelf edge when using hydrographic

©2018 American Geophysical Union. All rights reserved.

Accepted Article

data (Biddle et al., 2017). The noble gases indicate that the presence of GMW is widespread and persistent across the continental shelf.

Following the same method as with the oxygen isotope water mass fractions, we assess the spatial distribution of NG GMW by calculating column inventories between 150 - 700 m (Figure 4f). This depth range is selected in order to compare values more easily with the hydrographic GMW content, which cannot be used in the upper 150 m due to atmospheric interaction and SIM (Jenkins, 1999). This shows high NG GMW content along the front of PIIS (4.95 m) and in stations to the west, surrounding Thwaites (4.07 m) and at the western end of the zonal section south of Burke Island, where values are all higher than 1.9 m. The higher concentrations of NG GMW content in these locations is as previously reported (Nakayama et al., 2013; Biddle et al., 2017), and follows expected current patterns associated with geostrophic currents in the region (Wåhlin et al., 2013; Thurnherr et al., 2014). However, our data also show non-negligible quantities of GMW at the continental shelf edge with column inventories up to 1 m and mean values of 0.68 m. The central channel has mean column inventories of 0.77 m, similar to recent modelling studies (Nakayama et al., 2014). However, the eastern channel shows higher concentrations than models predict (up to 0.85 m) (Nakayama et al., 2014), although a 10 year model run recently showed an accumulated 4 m of GMW here (Nakayama et al., 2017).

5 Glacial meltwater from hydrographic tracers

The hydrographic tracers (Θ, S_A and $c(O_2)$) are used to calculate GMW content with OMPA (equation 2). End-members of mCDW, WW and GMW are used, as shown in Table 1. Biddle et al. (2017) discussed two variations of mCDW, namely mCDW and pseudo-CDW (pCDW). The pCDW endpoint refers to the precise properties on the mCDW-WW mixing line that are able to flow underneath PIIS to cause ocean basal melt and is specific to each season's characeteristics as the thermocline shoals or deepens (Biddle et al., 2017; Webber et al., 2017). The Θ-S_A-$c(O_2)$ mCDW endpoint will include GMW from different pCDW characteristics (Biddle et al., 2017). Since the NG mCDW endpoint does not vary between seasons or years, we use the mCDW endpoint for our hydrographic GMW calculations.

5.1 Comparison between GMW from noble gas and hydrographic tracers

The GMW content from noble gas tracers differs to the GMW content calculated from hydrographic tracers, which are shown for comparison in Figure 5. Close to PIIS (solid lines, Figure 5a), the hydrographic and noble gas tracers capture the same pattern of GMW presence but with NG GMW approximately 1 g kg^{-1} greater than GMW from hydrographic tracers (Figure 5b). This increases to nearly 2.5 g kg^{-1} at 200 m depth. A similar disparity between the two tracer methods is seen with distance from PIIS (all stations greater than 300 km from PIIS; dashed lines in Figure 5), where hydrographic tracer values of GMW drop to zero in the upper ocean column (grey line, Figure 5a). This results in an average offset of 2.71 g kg^{-1} between the two methods, but individual sampling locations between 150 - 400 m can differ up to 4.15 g kg^{-1} . If we use the NG GMW content as the representative content of GMW ($\pm$ 0.5 g kg^{-1}), this indicates that our hydrographic calculations have an average error of being nearly 3 g kg^{-1} lower than measured with noble gases.

Since these differences occur at a depth that correlates with the presence of WW (Biddle et al., 2017), it indicates an error with how we are defining our hydrographic water masses. We follow methods described by Jenkins et al. (2016) to correct our WW to a pure WW (pWW) to account for the presence of GMW within the hydrographic observations.

©2018 American Geophysical Union. All rights reserved.

Accepted Article

5.2 Adjusting for pWW

To obtain the pure WW (pWW) endpoint, we must first make some assumptions, following similar methods to Jenkins et al. (2016). WW is formed during the winter season, and is heavily influenced by atmospheric exchange and sea ice processes. In the continental shelf seas around Antarctica, this means that WW will reach the freezing point during sea ice formation. Using this knowledge, we extrapolate the existing WW endpoint down to the freezing temperature line (Figure 2a; red dot). For this dataset, this provides a new Θ and S_A endpoint for pWW of -1.86 °C and 34.32 g kg^{-1}, which is comparable to values used by Jenkins et al. (2016).

However, for the hydrographic GMW calculation, $c(O_2)$ is also used to define the water masses. To derive the $c(O_2)$ pWW endpoint is slightly more complex, as biological activity must be accounted for. The mean $c(O_2)$ saturation in the Amundsen Sea observed in 2014 of approximately 70 % is used as a lower bound (Biddle et al., 2017), and GMW is recalculated with $c(O_2)$ pWW values ranging from $c(O_2)$ saturation (100 %) to the lower bound of 70 % (Figure 2b). The observed mean oxygen saturation is used as the lower bound for the pWW as the admixture of mCDW-GMW will act to lower the dissolved oxygen concentration, therefore the pWW $c(O_2)$ endpoint should not be lower than what is observed for WW. Using this method, the $c(O_2)$ value used for the pWW endpoint is 295 μmol kg^{-1}, at 80 % saturation.

5.3 Improvement of glacial meltwater calculation from hydrographic tracers

The GMW content is recalculated using the hydrographic tracers and mCDW, pWW and GMW endpoints (Figure 2a,b, Figure 6). Previously, the hydrographic calculation presented in Section 5.1 performed reasonably well in front of PIIS (Figure 5a), but both here and at the continental shelf edge showed a significant offset from the NG GMW content between 150 - 300 m. With the new pWW endpoint, the GMW content is improved and differences between the GMW content from hydrographic tracers or noble gas tracers between 150 - 700 m are on average less than 1.06 g kg^{-1} across the whole region sampled, with no consistent offset (Figure 6b). This is close to the accepted reliability of the hydrographic GMW calculation ($\pm$1 g kg^{-1}) and so can be considered a good improvement in the hydrographic GMW calculation.

The change in the column inventories (calculated as before) from using WW to using pWW averages to an increase of about 0.53 m GMW on each station, but it does not significantly change the spatial variability in GMW content (Figure 7). The average difference between the hydrographic GMW and NG GMW column inventories is 11 cm ($<$ 5% of the mean column inventory values) for comparable stations, with the hydrographic GMW column inventories showing slightly higher values.

6 Distribution of glacial meltwater in the Amundsen Sea

This correction to the hydrographic GMW calculation results in the ability to improve our hydrographic GMW calculations, resulting in an increase in the spatial resolution of GMW content compared to noble gas tracers. This gives a more detailed map of GMW content (Figure 7). As shown by the NG GMW content and as previously described by (Biddle et al., 2017), the highest concentrations of GMW are found in front of PIIS (5.23 m) and to the west around Thwaites Ice Shelf (4.48 m). In both these locations, the highest value is found at the station furthest to the west, which correlates with the known location of the strongest glacial outflow from PIIS (Jenkins et al., 2010; Thurnherr et al., 2014). Similarly, we can assume that the high GMW value at the west of Thwaites indicates the likely strongest glacial outflow in that location, following geostrophic currents underneath the ice shelf.

©2018 American Geophysical Union. All rights reserved.

Accepted Article

Across the zonal section to the south of Burke Island, the GMW content increases towards the west with values up to 1.98 m (section C; Figure 7). Column integrals at the eastern end of this section are the lowest values (0.35 m) calculated across the continental shelf. North and east of Burke Island, there is a persistent signature along the eastern channel. On average, column inventories here are 1.33 m, increasing towards the continental shelf edge. These values were not shown by Biddle et al. (2017) due to the likelihood of a secondary source of GMW than PIIS in this region: this GMW signature could be coming from the Bellingshausen Sea further to the east (Zhang et al., 2016), or local melt from Abbot Ice Shelf or Cosgrove Ice Shelf.

A significant change to previous GMW calculations using hydrographic tracers is that there is now a GMW presence at the edge of the continental shelf (sections A and B; Figure 7). In the central channel, this is 0.63 m on average, with only a small variation across the channel. However, in the eastern channel, the column inventories are all greater than 0.7 m, with an average of 1.08 m. Towards the western edge of this channel section, the column inventories are consistently over 1.09 m of GMW.

By combining the GMW content with velocity fields measured by the LADCP, the distribution of GMW can be related to possible pathways. We use the four zonal sections (Figure 1) to describe the GMW depth distribution and meltwater pathways, with the velocity fields rotated to along and across channel directions for each section (Figures 8,9). Advection from PIIS off shelf is of most interest for this study and so only the along channel velocities are shown, with across channel velocities in supplementary material (Figure S6).

All four sections show that the GMW is typically only present above the 27.72 isopycnal, which shoals from the seabed in front of PIIS (Figure 8a) to approximately 400 m depth at the continental shelf edge (Figure 9a,c). The mean GMW content between the 27.6 and 27.7 isopycnals reduces by only 0.5 g kg^{-1} between PIIS and the continental shelf edge (3.77 g kg^{-1} to 3.28 g kg^{-1}), whilst the signature of GMW between 100 - 200 m reduces dramatically with distance from PIIS from an average of 12.6 g kg^{-1} to 3.18 g kg^{-1}. At the continental shelf edge, at distance from the ice shelf, the GMW content is approximately evenly distributed between 150 - 400 m. The hydrographic and NG GMW content match well below the 27.7 isopycnal across all of the sections, except for the eastern end of the eastern channel (Figure 9c). This is due to a strong presence of the offshore Upper CDW (UCDW) component, which is less saline and warmer than the Lower CDW component and so appears as a false GMW signature. This false GMW signature is henceforth ignored in this discussion.

Directly in front of PIIS (Figure 8a), the hydrographic tracers capture small scale changes in GMW content in the upper 300 m, likely caused by the energetic export of highly buoyant meltwater from the ice shelf (Garabato et al., 2017). The GMW content is concentrated to the upper 600 m and towards the western end of the section (Figure 8a). A largely off-shelf flow coincides with the high GMW content in the western portion of the section, with a stronger core at 400 m that also has some westward directionality (3.6 km along section; Figures 8a,b,S1). This agrees with previous studies of the transport of GMW in front of PIIS (Jenkins et al., 2010; Thurnherr et al., 2014).Below 900 m depth, the GMW content appears to increase from a minimum of 1.14 g kg^{-1} between 700 - 900 m to 2.52 g kg^{-1}. Although there is one noble gas sample taken at 1000 m depth at about 12 km distance along the section that contains 2.26 g kg^{-1}, there is currently not enough evidence to confirm whether this increase at depth is a real feature.

The zonal section to the south of Burke Island (Section C; Figure 1, Figure 8c) is approximately 200 km from the front of the ice shelf. The eastern end of the section occurs over a shallow sill that separates the channel to the east of Burke Island and the main Pine Island Trough (bottom depth reported as 278 m). At this distance from PIIS,

©2018 American Geophysical Union. All rights reserved.

Accepted Article

there is still a stronger surface expression of GMW and the mean value of GMW between 100 - 200 m at the western end of the section is 5.5 g kg^{-1}. There is a second core of higher GMW content (5.85 g kg^{-1}) towards the western side of Pine Island Trough at 400 m depth. The lowest column inventories are found at the eastern end of this section (Figure 7) and this is visible in the low GMW content signature evident throughout the water column (Figure 8c). Across the section there are two clear flow regimes: a strong off-shelf flow on the western end of the section, and a strong toward-PIIS flow at the eastern side (Figure 8d). The strongest off-shelf flow occurs at 45 km distance across the section and, combined with the across channel velocity, indicates flow towards the west along the coast line and/or off-shelf. The core of the strong off-shelf flow correlates well with the core of higher GMW content (Figure 8c,d).

At the edge of the continental shelf, there is no significant increase in GMW content towards the surface (Figure 9a,c). Across the central channel, 535 km from PIIS, the GMW content is lower than in the eastern channel and all values below 150 m depth are less than 3.9 g kg^{-1} (Figure 9a). This section is also different to the previous sections, as the highest GMW values are found on the eastern side of the channel (50 km section distance, Figure 9a). There is a stronger on-shelf flow at the eastern end of the section, whilst the off-shelf flow is spread across the western portion (Figure 9b). The water with the higher GMW content to the east is flowing on-shelf (Figure 9a,b), which suggests that the GMW here may have a source elsewhere. It could be recirculated PIIS GMW, either flowing westwards along the continental shelf edge from the eastern channel, or from the previously modelled and observed circulation patterns at the shelf edge of the central channel (Assmann et al., 2013).

The zonal section across the eastern channel (Figure 9c) is 430 km from PIIS and is the longest section included in this analysis. Except for the anomalous UCDW GMW signature, GMW content here is typically below 5 g kg^{-1}, with higher values towards the western edge of the section. In the first 80 km of the section there is an elevated surface signature (values up to 4.68 g kg^{-1}), and another increase in GMW content at about 300 m depth along the same isopycnal as the GMW signature at depth on section C (Figures 8c, 9c). There is a strong off-shelf flow that characterises much of the section (from 0-160 km), with the eastern end of the section showing an on-shelf flow dominated by a strong eddy-type feature that is associated with the UCDW signature. The location of higher GMW content (Figure 9c) is flowing off-shelf, implying that the GMW identified likely has an origin from the Amundsen Sea.

Our analysis has confirmed previous studies that focused on GMW pathways directly in front of PIIS and has strengthened the analysis by Biddle et al. (2017) that the strongest GMW outflow occurs at the western end of PIIS. The GMW then flows along the coast to the west, as seen in the zonal section south of Burke Island (Figure 8c,d). We have also revealed new observations about the GMW at the continental shelf edge, showing off-shelf flow of GMW in the eastern channel, and possible recirculation in the central channel (Figure 9).

7 Discussion

We have presented new datasets from the iSTAR 2014 research cruise, including oxygen isotope ratios and noble gas concentrations. The oxygen isotope ratios provide estimates of SIM and MWI to the water column. We detected a strong signature of sea ice growth across the continental shelf and sea ice melt at the continental shelf edge, which agrees with satellite observations of sea ice concentrations in the Amundsen Sea (Stammerjohn et al., 2015). In particular, the MWI distribution highlights the increase in freshwater towards the western end of the eastern channel. Overall, the MWI was on average 4.8 m greater than the column inventories of GMW, possibly indicating either a longer res-

©2018 American Geophysical Union. All rights reserved.

Accepted Article

idence time associated with oxygen isotopes or a high precipitation content in the water column, which has been reported for this region before (Lenaerts et al., 2012).

The use of noble gases to quantify GMW provides reliable estimates that are used as a ground-truth for our other water mass calculations. The noble gases revealed a persistent signature between 150 - 400 m depth of GMW across all of the stations sampled, which has not been reported in the eastern Amundsen Sea before. It is likely that close to PIIS there is a significant GMW content that is excluded from this study between the surface and 150 m, but due to atmospheric effects these depths have been excluded. This indicates our column inventories of GMW content are likely under-estimates. GMW content from the noble gas concentrations showed non-negligible values at the edge of the continental shelf, up to 535 km away from PIIS. These column inventories also showed GMW in the eastern channel for the first time using observational data.

The GMW content from NG was used to improve our calculations of GMW from hydrographic tracers (temperature, salinity and dissolved oxygen). The differences between using NG or hydrographic tracers to calculate GMW content highlighted an error in the setting of the WW endpoint, as previously the in-situ hydrographic observations were used to specify this endpoint. The GMW content from NG showed that GMW exists at the depth of WW (150 - 350 m), and so the observed 'Winter Water' content must first be corrected for the presence of GMW, creating the 'pure Winter Water' (pWW) endpoint. Whilst Jenkins et al. (2016) used the concept of pWW, we have shown the quantifiable difference using this endpoint makes when compared with the GMW from noble gases.

When the improved WW endpoint is used in the revised hydrographic calculation, the differences between the two methods decrease significantly and the GMW signature is traced as it travels from PIIS. The strong surface (150 m) expression rapidly decreases, but is still visible in the section across Pine Island Trough approximately 200 km from PIIS. At the continental shelf edge, there is no significant signature of GMW at 150 m depth. A second signature of GMW between 400 - 600 m was recognisable across all stations, between the isopycnals of 27.5 and 27.7. This was seen clearly in the central Pine Island Trough, flowing off-shelf, and was the main contributor to the GMW column inventories at the continental shelf edge.

By combining the GMW patterns with observed velocity profiles, we were able to infer the meltwater pathways. This confirms the previously reported pathway of GMW from the western side of PIIS, flowing along the coastline to the west and towards the north, off-shelf. It supports both previous observations (Nakayama et al., 2013; Biddle et al., 2017) and modeling studies (Nakayama et al., 2014, 2017). The GMW signature observed at the western end of the eastern channel was shown to be flowing off-shelf, which has not been reported in observations as a pathway for GMW previously. The model results presented by Nakayama et al. (2014, 2017) predicted that the central channel should contain higher GMW content than the eastern channel, yet our data show greater values in the eastern channel, with the GMW content in the central channel associated with a recirculation and GMW flowing on-shelf. This emphasizes our need to improve the understanding of the transport across these channels at the continental shelf edge, and how and where GMW flows off the continental shelf.

Whilst the use of oxygen isotope ratios and noble gas concentrations are critical for identifying sea ice melt and reliable GMW content, the improvements we have made to the hydrographic GMW content indicate that when these tracers aren't available we are still able to make a good estimate of it. If noble gas concentrations are not available for ground-truth, we can use the assumptions that the pWW endpoint can be extrapolated from the existing in-situ WW to the freezing temperature with associated salinity and that the oxygen concentrations will be undersaturated (at 80% in the eastern Amundsen Sea). The user can also run Monte-Carlo simulations with small perturbations of their

©2018 American Geophysical Union. All rights reserved.

Accepted Article

new pWW endpoints to determine the sensitivity of their results. As our pWW endpoints in Θ, S_A and $c(O_2)$ are similar to those used by Jenkins et al. (2016) to the west of PIIS in front of Dotson Ice Shelf for 2014 data, this suggests that the pWW endpoint used here is reliable over a reasonable geographic area (approximately 20 ° longitude), but is likely to be variable on timescales greater than a year.

The noble gas sampling locations where there are larger differences between the NG and hydrographic GMW contents may indicate the effects of other processes affecting the tracer signatures, in particular biological activity. The presence of GMW is often associated with biological productivity (St-Laurent et al., 2017), which can increase the concentration of dissolved oxygen. Due to the admixture of mCDW-GMW having lower $c(O_2)$ values than WW, the biological productivity skews the apparent GMW content towards lower values. Further work is required to understand the relationship between glacial meltwater and biological activity – does it support productivity and respiration, and how does this ratio vary across the continental shelf? In addition, this dataset has revealed more detail on the spatial and vertical distribution of GMW that can be used to validate existing circulation models for this region.

8 Conclusions

We have demonstrated the value of oxygen isotope ratios and noble gas concentrations in determining freshwater distribution across Amundsen Sea. Noble gas concentrations enable a reliable calculation of GMW content that is used as a ground-truth for hydrographic water mass calculations to be tuned to, using the pWW endpoint.

Our new observations of meltwater pathways across the eastern Amundsen Sea show the persistent presence of GMW between 150 - 400 m across the entire continental shelf sampled. Combining GMW content with velocity fields show strong outflows at the westernmost stations of both PIIS and Thwaites Ice Shelf, with the GMW flowing off-shelf and along the coast to the west. We have also shown that an important location of GMW export off the continental shelf exists in the eastern channel.

Finally, the pWW endpoint should be used for future GMW calculations, even when noble gas tracers are not available for ground-truthing. The extrapolation of the in-situ WW endpoint to the freezing temperature and salinity, with an undersaturated oxygen concentration provides a more reliable GMW content than the observed WW endpoint.

Acknowledgments

We acknowledge funding for the Ocean2ice project at UEA from the UK Natural Environment Research Councils iSTAR programme through grant NE/J005703/1, which supported KJH and LCB as well as the ship-based campaign. We thank all involved with RRS James Clark Ross cruise 294 for making these observations possible. We acknowledge US National Science Foundation Award #1341630 for support of BL and for noble gas analysis. Noble gas samples are available from the IEDA Earthchem Library (https://ecl.earthchem.org/view.php?id=1152). All other data described here can be obtained from the British Oceanographic Data Centre www.bodc.ac.uk. LCB is now supported by a Wallenberg Academy Fellowship of S. Swart (WAF 2015.0186).

References

Arneborg, L., Wåhlin, A. K., Björk, G., Liljebladh, B., & Orsi, A. H. (2012). Persistent inflow of warm water onto the central Amundsen shelf. *Nature Geoscience*, *5*(12), 876–880. doi: 10.1038/ngeo1644

Assmann, K. M., Jenkins, A., Shoosmith, D. R., Walker, D. P., Jacobs, S. S., & Nicholls, K. W. (2013). Variability of Circumpolar Deep Water trans-

©2018 American Geophysical Union. All rights reserved.

Accepted Article

port onto the Amundsen Sea Continental shelf through a shelf break trough. *Journal of Geophysical Research: Oceans*, *118*(12), 6603–6620. doi: 10.1002/2013JC008871

Beaird, N., Straneo, F., & Jenkins, W. (2015). Spreading of Greenland meltwaters in the ocean revealed by noble gases. *Geophysical Research Letters*, 1–9. doi: 10.1002/2015GL065003.Abstract

Biddle, L. C., Heywood, K. J., Kaiser, J., & Jenkins, A. (2017). Glacial meltwater identification in the Amundsen Sea. *Journal of Physical Oceanography*, *47*, JPO–D–16–0221.1. doi: 10.1175/JPO-D-16-0221.1

Bintanja, R., Oldenborgh, G. J. V., Drijfhout, S. S., Wouters, B., & Katsman, C. A. (2013). Important role for ocean warming and increased ice-shelf melt in Antarctic sea-ice expansion. *Nature Geoscience*, *6*(4), 1–4. doi: 10.1038/ngeo1767

Garabato, A. C. N., Forryan, A., Dutrieux, P., Brannigan, L., Biddle, L. C., Heywood, K. J., ... Kimura, S. (2017). Vigorous lateral export of the meltwater outflow from beneath an Antarctic ice shelf. *Nature*, *542*(7640), 219–222. doi: 10.1038/nature20825

Heywood, K. J., Biddle, L. C., Boehme, L., Dutrieux, P., Fedak, M., Jenkins, A., ... Webber, B. G. M. (2016). Between the Devil and the Deep Blue Sea: The Role of the Amundsen Sea Continental Shelf in Exchanges Between Ocean and Ice Shelves. *Oceanography*, *29*.

Hohmann, R., Schlosser, P., Jacobs, S., Ludin, A., & Weppernig, R. (2002). Excess helium and neon in the southeast pacific: Tracers for glacial meltwater. *Journal of Geophysical Research: Oceans*, *107*(C11), 19-1-19-14. doi: 10.1029/2000JC000378

Huhn, O., Hattermann, T., Davis, P. E. D., Dunker, E., Hellmer, H. H., Nicholls, K. W., ... Sltenfu, J. (2018). Basal melt and freezing rates from first noble gas samples beneath an ice shelf. *Geophysical Research Letters*, *45*(16), 8455-8461. doi: 10.1029/2018GL079706

IOC, SCOR, & IAPSO. (2010). The international thermodynamic equation of seawater - 2010: Calculation and use of thermodynamics properties. In *Intergovernmental oceanographic commission, manuals and guides no. 56* (p. 196). UNESCO (English).

Jacobs, S. S., & Giulivi, C. F. (2010). Large Multidecadal Salinity Trends near the PacificAntarctic Continental Margin. *Journal of Climate*, *23*(17), 4508–4524. doi: 10.1175/2010JCLI3284.1

Jacobs, S. S., Hellmer, H. H., & Jenkins, A. (1996). Antarctic ice sheet melting in the Southeast Pacific. *Geophysical Research Letters*, *23*(9), 957–960.

Jacobs, S. S., Jenkins, A., Giulivi, C. F., & Dutrieux, P. (2011). Stronger ocean circulation and increased melting under Pine Island Glacier ice shelf. *Nature Geoscience*, *4*(8), 519–523. doi: 10.1038/ngeo1188

Jacobs, S. S., Jenkins, A., Hellmer, H. H., Giulivi, C. F., Nitsche, F., Huber, B., & Guerrero, R. (2012). The Amundsen Sea and the Antarctic Ice Sheet. *Oceanography*, *25*(3), 154–163. doi: http://dx.doi.org/10.5670/oceanog.2012.90

Jenkins, A. (1999). The impact of melting ice on ocean waters. *Journal of physical oceanography*(3), 2370–2381.

Jenkins, A., Dutrieux, P., Jacobs, S. S., McPhail, S. D., Perrett, J. R., Webb, A. T., & White, D. (2010, jun). Observations beneath Pine Island Glacier in West Antarctica and implications for its retreat. *Nature Geoscience*, *3*(7), 468–472. doi: 10.1038/ngeo890

Jenkins, A., Shoosmith, D., Dutrieux, P., Jacobs, S., Kim, T. W., & Lee, S. H. (2016). West Antarctic Ice Sheet retreat in the Amundsen Sea driven by decadal oceanic variability. *Nature Geoscience*. doi: 10.1038/s41561-018-0207-4

Jourdain, N. C., Mathiot, P., Merino, N., Durand, G., Le Sommer, J., Spence, P., ...

©2018 American Geophysical Union. All rights reserved.

Accepted Article

Madec, G. (2017). Ocean circulation and sea-ice thinning induced by melting ice shelves in the Amundsen Sea. *Journal of Geophysical Research: Oceans*, *122*(3), 2550-2573. doi: 10.1002/2016JC012509

Kim, I., Hahm, D., Rhee, T. S., Kim, T. W., Kim, C. S., & Lee, S. H. (2016). The distribution of glacial meltwater in the Amundsen Sea, Antarctica, revealed by dissolved helium and neon. *Journal of Geophysical Research: Oceans*, *121*(3), 1654–1666. doi: 10.1002/2015JC011211

Lenaerts, J. T. M., van den Broeke, M. R., van de Berg, W. J., van Meijgaard, E., & Kuipers Munneke, P. (2012). A new, high-resolution surface mass balance map of Antarctica (19792010) based on regional atmospheric climate modeling. *Geophysical Research Letters*, *39*(4). Retrieved from `https://agupubs.onlinelibrary.wiley.com/doi/abs/10.1029/2011GL050713` doi: 10.1029/2011GL050713

Loose, B., Garabato, A. C. N., Schlosser, P., Jenkins, W. J., Vaughan, D., & Heywood, K. J. (2018). Evidence of an active volcanic heat source beneath the Pine Island Glacier. *Nature Communications*(9), 1–9. doi: 10.1038/s41467-018-04421-3

Loose, B., & Jenkins, W. J. (2014). The five stable noble gases are sensitive unambiguous tracers of glacial meltwater. *Geophysical Research Letters*, *41*, 2835–2841. doi: 10.1002/2013GL058804.Received

Loose, B., Jenkins, W. J., Moriarty, R., Brown, P., Jullion, L., Naveira Garabato, A. C., ... Meredith, M. P. (2016, aug). Estimating the recharge properties of the deep ocean using noble gases and helium isotopes. *Journal of Geophysical Research: Oceans*, *121*(8), 5959–5979. doi: 10.1002/2016JC011809

Loose, B., Schlosser, P., Smethie, W. M., & Jacobs, S. (2009). An optimized estimate of glacial melt from the Ross Ice Shelf using noble gases, stable isotopes, and CFC transient tracers. *Journal of Geophysical Research: Oceans*, *114*(8), 1–15. doi: 10.1029/2008JC005048.

Lott, D. E. (2001). Improvements in noble gas separation methodology: A nude cryogenic trap. *Geochemistry, Geophysics, Geosystems*, *2*. doi: 10.129/2001GC000202

Mallett, H. K. W., Boehme, L., Fedak, M., Heywood, K. J., Stevens, D. P., & Roquet, F. (2018). Variation in the distribution and properties of circumpolar deep water in the eastern amundsen sea, on seasonal timescales, using seal-borne tags. *Geophysical Research Letters*, *45*(10), 4982-4990. doi: 10.1029/2018GL077430

Meredith, M. P., Brandon, M. a., Wallace, M. I., Clarke, A., Leng, M. J., Renfrew, I. a., ... King, J. C. (2008). Variability in the freshwater balance of northern Marguerite Bay, Antarctic Peninsula: Results from δ18O. *Deep Sea Research Part II: Topical Studies in Oceanography*, *55*(3-4), 309–322. doi: 10.1016/j.dsr2.2007.11.005

Nakayama, Y., Menemenlis, D., Schodlok, M., & Rignot, E. (2017). Amundsen and bellingshausen seas simulation with optimized ocean, sea ice, and thermodynamic ice shelf model parameters. *Journal of Geophysical Research: Oceans*, *122*(8), 6180-6195. doi: 10.1002/2016JC012538

Nakayama, Y., Schröder, M., & Hellmer, H. (2013). From circumpolar deep water to the glacial meltwater plume on the eastern Amundsen Shelf. *Deep Sea Research Part I: Oceanographic Research Papers*, *77*, 50–62. doi: 10.1016/j.dsr.2013.04.001

Nakayama, Y., Timmermann, R., Rodehacke, C. B., Schröder, M., & Hellmer, H. H. (2014). Modeling the spreading of glacial meltwater from the Amundsen and Bellingshausen Seas. *Geophysical Research Letters*, 7942–7949. doi: 10.1002/2014GL061600.1.

Payne, A. J., Vieli, A., Shepherd, A. P., Wingham, D. J., & Rignot, E. (2004). Recent dramatic thinning of largest west antarctic ice stream triggered by oceans.

©2018 American Geophysical Union. All rights reserved.

Accepted Article

Geophysical Research Letters, *31*(23). doi: 10.1029/2004GL021284

Price, M. R., Heywood, K. J., Nicholls, K. W., Ice-shelf, K. W. N., & Ice, F. (2008). Ice-shelf – ocean interactions at Fimbul Ice Shelf , Antarctica from oxygen isotope ratio measurements. *Ocean Science*, *4* , 89–98.

Pritchard, H. D., Ligtenberg, S. R. M., Fricker, H. A., Vaughan, D. G., van den Broeke, M. R., & Padman, L. (2012). Antarctic ice-sheet loss driven by basal melting of ice shelves. *Nature*, *484*(7395), 502–5. doi: 10.1038/nature10968

Randall-Goodwin, E., Meredith, M. P., Jenkins, A., Yager, P. L., Sherrell, R. M., Abrahamsen, E. P., ... Stammerjohn, S. E. (2015). Freshwater distributions and water mass structure in the Amundsen Sea Polynya region, Antarctica. *Elementa: Science of the Anthropocene*, *3*(1). doi: 10.12952/journal.elementa.000065

Schmidtko, S., Heywood, K. J., Thompson, A. F., & Aoki, S. (2014). Multidecadal warming of Antarctic waters. *Science*, *346*(6214), 1227 LP – 1231. doi: 10 .1126/science.1256117

Shepherd, A., Fricker, H. A., & Farrell, S. L. (2018). Trends and connections across the Antarctic cryosphere. *Nature*, *558*, 223–232. doi: 10.1038/s41586-018-0171 -6

Silvano, A., Rintoul, S. R., Peña-Molino, B., Hobbs, W. R., Wijk, E. V., Aoki, S., ... Williams, G. D. (2018). Freshening by glacial meltwater enhances melting of ice shelves and reduces formation of Antarctic Bottom Water. *Science Advances*, *4* , 1–12. doi: 10.1126/sciadv.aap9467

Stammerjohn, S. E., Maksym, T., Massom, R. a., Lowry, K. E., Arrigo, K. R., Yuan, X., ... Yager, P. L. (2015). Seasonal sea ice changes in the Amundsen Sea, Antarctica, over the period of 19792014. *Elementa: Science of the Anthropocene*, *3*(1). doi: 10.12952/journal.elementa.000055

Stanley, R. H. R., Jenkins, W. J., Lott, D. E., & Doney, S. C. (2009). Noble gas constraints on air-sea gas exchange and bubble fluxes. *Journal of Geophysical Research*, *114* , 1–14. doi: 10.1029/2009JC005396

St-Laurent, P., Yager, P. L., Sherrell, R. M., Stammerjohn, S. E., & Dinniman, M. S. (2017). Pathways and supply of dissolved iron in the Amundsen Sea (Antarctica). *Journal of Geophysical Research: Oceans*, *122*(9), 7135-7162. doi: 10.1002/2017JC013162

Thoma, M., Jenkins, A., Holland, D., & Jacobs, S. (2008). Modelling Circumpolar Deep Water intrusions on the Amundsen Sea continental shelf, Antarctica. *Geophysical Research Letters*, *35*(18), L18602. doi: 10.1029/2008GL034939

Thurnherr, A., Jacobs, S. S., Dutrieux, P., & Giulivi, C. F. (2014). Export and circulation of ice cavity water in Pine Island Bay, West Antarctica. *Journal of Geophysical Research : Oceans*, 1754–1764. doi: 10.1002/2013JC009307

Wåhlin, A. K., Kalén, O., Arneborg, L., Björk, G., Carvajal, G. K., Ha, H. K., ... Stranne, C. (2013). Variability of Warm Deep Water Inflow in a Submarine Trough on the Amundsen Sea Shelf. *Journal of Physical Oceanography*, *43*(10), 2054–2070. doi: 10.1175/JPO-D-12-0157.1

Walker, D. P., Brandon, M. A., Jenkins, A., Allen, J. T., Dowdeswell, J. A., & Evans, J. (2007, jan). Oceanic heat transport onto the Amundsen Sea shelf through a submarine glacial trough. *Geophysical Research Letters*, *34*(2), L02602. doi: 10.1029/2006GL028154

Webber, B. G. M., Heywood, K. J., Stevens, D. P., Dutrieux, P., Abrahamsen, E. P., Jenkins, A., ... Kim, T. W. (2017). Mechanisms driving variability in the ocean forcing of Pine Island Glacier. *Nature Communications*, *8*, 1–8. doi: 10.1038/ncomms14507

Weiss, R., Östlund, H., & Craig, H. (1979). Geochemical studies of the Weddell Sea. *Deep Sea Research Part A. Oceanographic Research Papers*, *26*(10), 1093 - 1120. doi: https://doi.org/10.1016/0198-0149(79)90059-1

Zhang, X., Thompson, A. F., Flexas, M. M., Roquet, F., & Bornemann, H. (2016).

©2018 American Geophysical Union. All rights reserved.

Circulation and meltwater distribution in the Bellingshausen Sea : From shelf break to coast. *Geophysical Research Letters*, *43*, 6402–6409. doi: 10.1002/2016GL068998.Abstract

Accepted Article

©2018 American Geophysical Union. All rights reserved.

Accepted Article

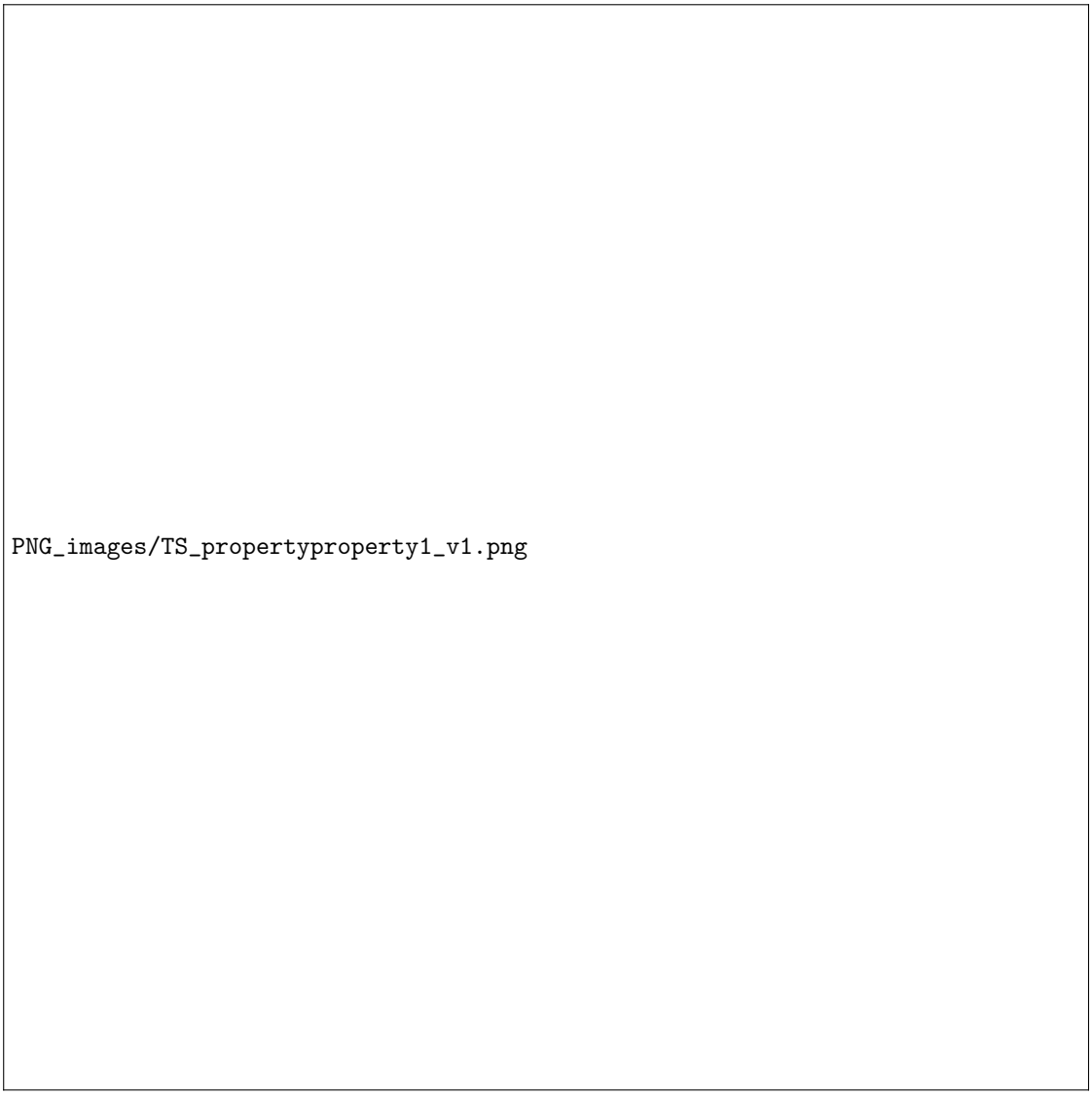

Figure 2. Property-property diagrams showing (a) Θ-S_{A}, (b) S_{A}-$c(O_2)$. Inset on each figure shows the mixing direction for mCDW with WW (green) and GMW (dark blue). The grey dots are all of the CTD data from the continental shelf (pink dots in Figure 1), all other colors are consistent with Figure 1. The pink circles highlight the mCDW endpoint. The solid red dot shows the pWW endpoint and pink squares in (b) show the different $c(O_2)$ saturation values used.

©2018 American Geophysical Union. All rights reserved.

Accepted Article

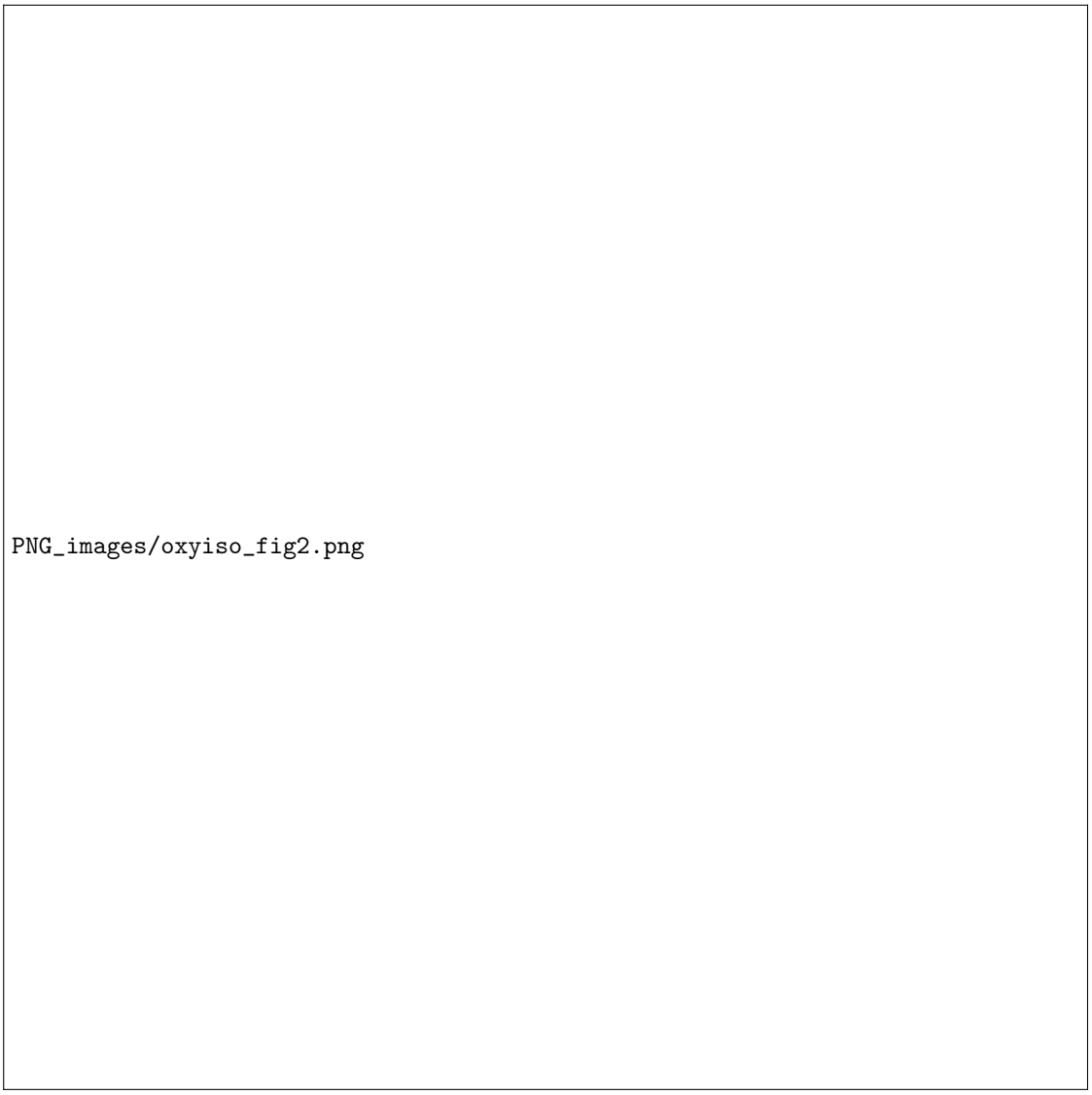

Figure 3. Figures showing S_A-$\delta^{18}O$ relationship (a), and distribution of mCDW, SIM and MWI (b)-(d). (a) All $\delta^{18}O$ data from the Amundsen Sea. Red circles show mCDW endpoint, and the inset shows mixing direction between mCDW and SIM (green arrow) or MWI (blue arrow). (b) Vertical distribution for all data points across Amundsen Sea of mCDW (red), SIM (green) and MWI (blue) as a percentage of maximum observed fractions. Values are shown for -20, 20, 40, 60 and 80 % in g kg^{-1} for SIM and MWI and as a fraction of 1 for mCDW. (c) Vertically integrated SIM (top 500 m). Negative values indicate sea ice growth. (d) Vertically integrated MWI in the top 500 m.

©2018 American Geophysical Union. All rights reserved.

Accepted Article

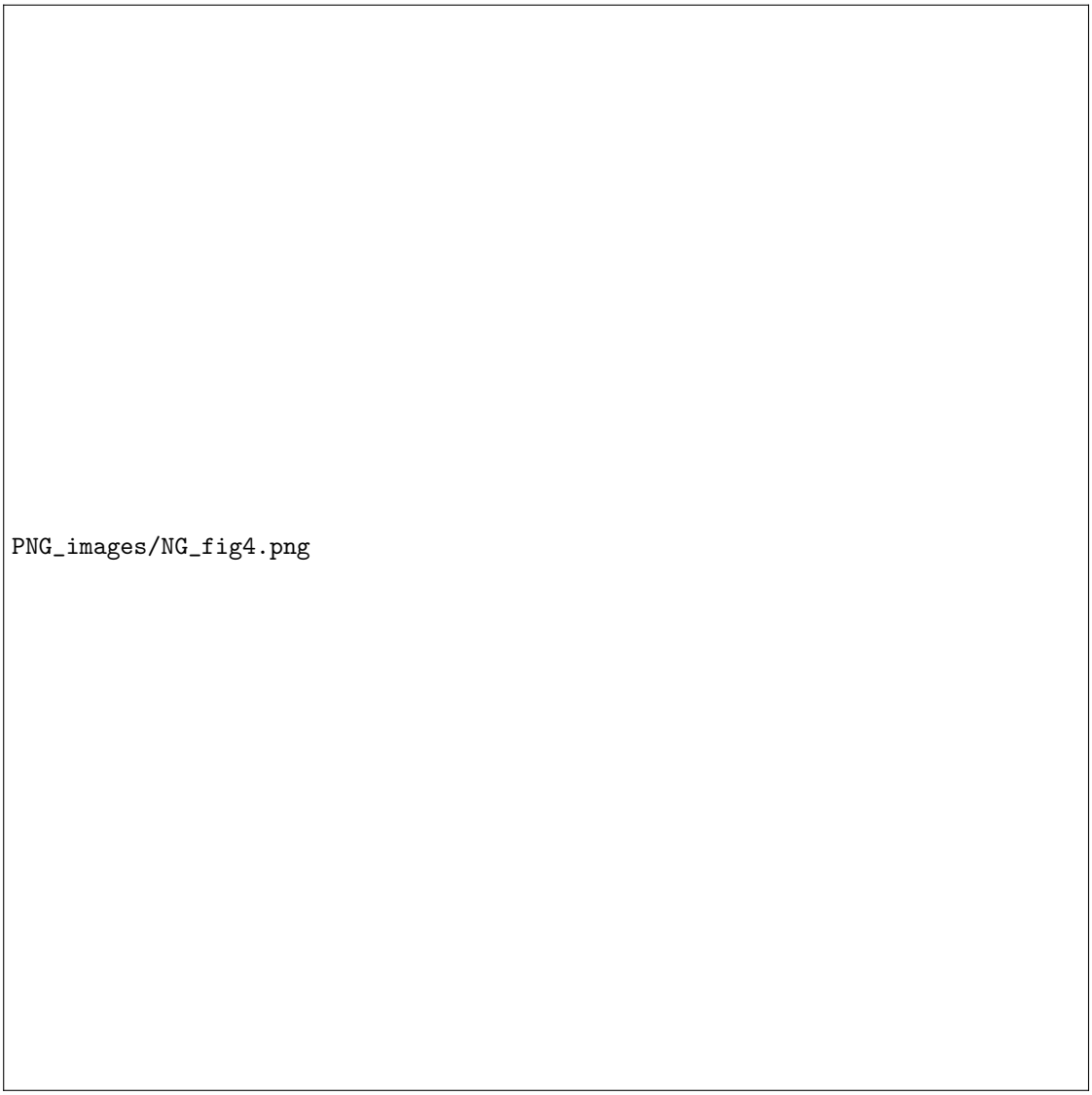

Figure 4. Figures showing S_{A}-$c(Ar)$ relationship colored by Θ(a), and $c(Ar)$- $c(Ne)$, $c(Kr)$ and $C(Xe)$ (b)-(d), colored by S_{A}. Red circles show mCDW endpoint, and the inset shows mixing direction between mCDW and AEW (green arrow) or GMW (blue arrow). (e) Vertical distribution for all data points across Amundsen Sea of mCDW (red), AEW (green) and GMW (blue) as a percentage of maximum observed fractions. Values for 20, 40, 60 and 80 % are shown in g kg^{-1} for GMW and as a fraction of 1 for AEW and mCDW. (f) Vertically integrated GMW (between 150 - 700 m).

©2018 American Geophysical Union. All rights reserved.

Accepted Article

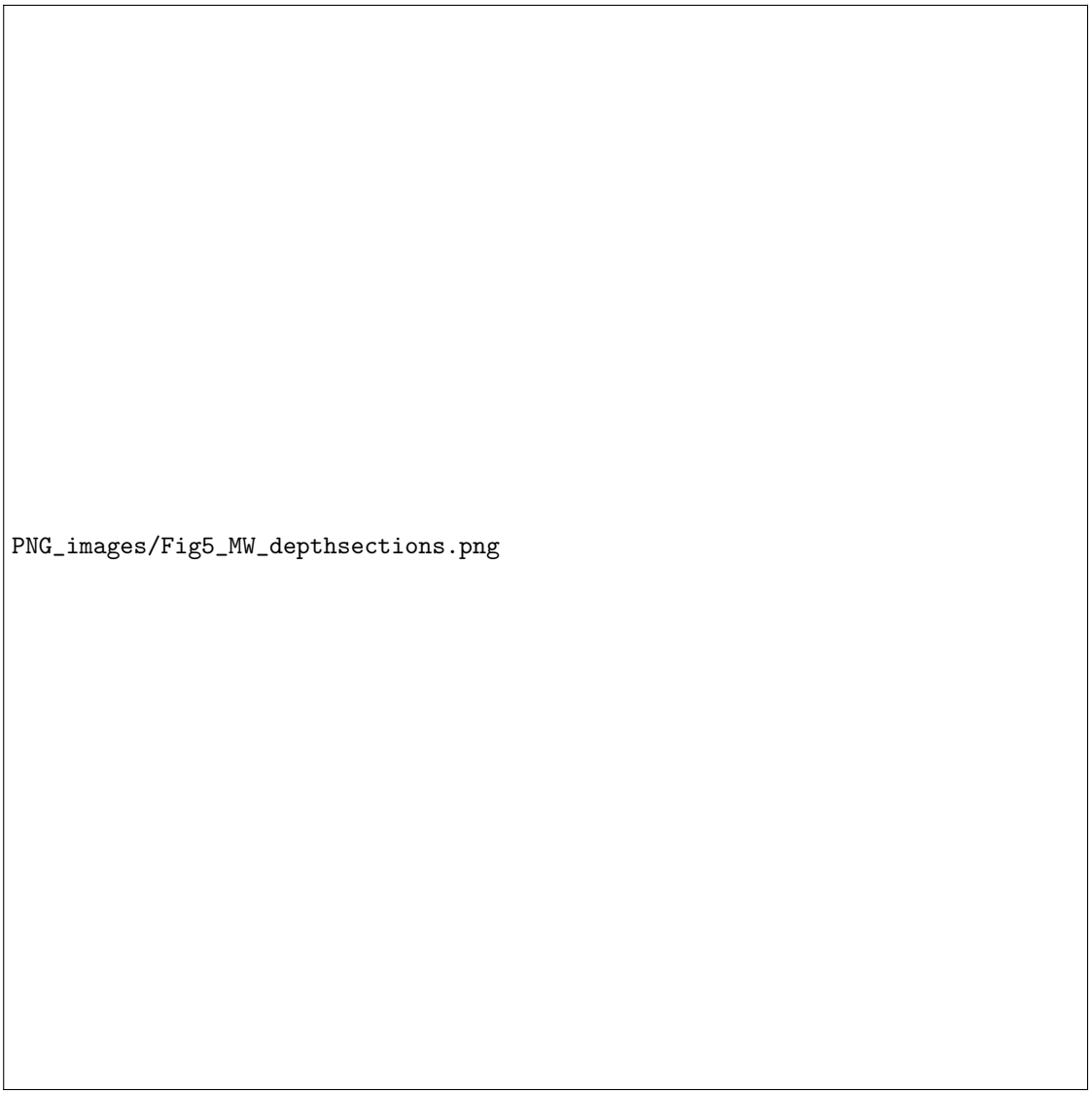

Figure 5. Vertical depth profiles of (a) GMW content from NG tracers (red) and hydrogaphic tracers (grey) and (b) the difference (GMW_{NG}-$GMW_{T,S,O}$) between the two methods. Dashed lines and dots represent the mean or point values of GMW content at the continental shelf edge (>300 km from PIIS) and solid lines and squares show the mean or point values of GMW content directly in front of PIIS (<100 km).

©2018 American Geophysical Union. All rights reserved.

Accepted Article

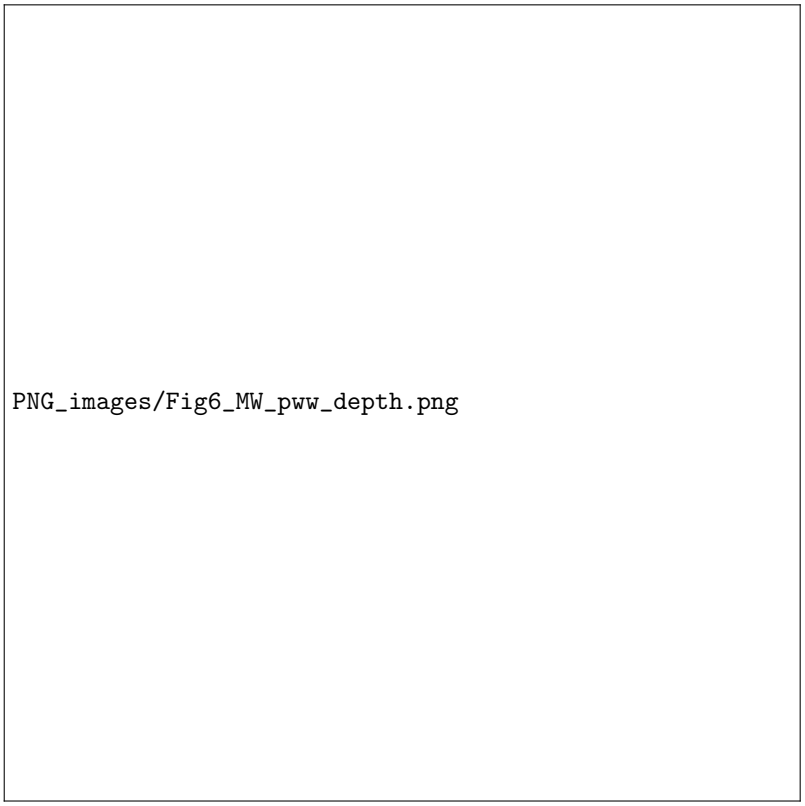

Figure 6. Vertical depth profiles of (a) GMW content from NG tracers (red) and hydrogaphic tracers, using the pWW endpoint (grey) and (b) the difference (GMW_{NG}-$GMW_{T,S,O}$) between the NG method and pWW method. Dashed lines and dots represent the mean or point values of GMW content at the continental shelf edge (>300 km from PIIS) and solid lines and squares show the mean or point values of GMW content directly in front of PIIS (<100 km).

©2018 American Geophysical Union. All rights reserved.

Accepted Article

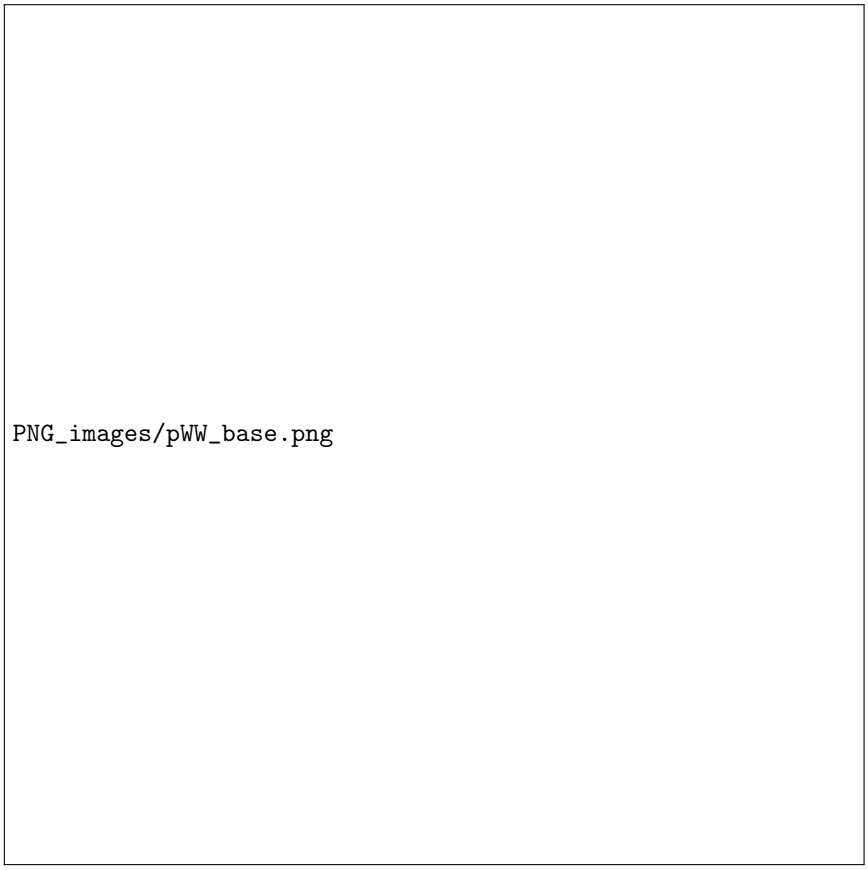

Figure 7. Map of vertically integrated GMW content (between 150 - 700 m) in the eastern Amundsen Sea, calculated using Θ, S_A and $c(O_2)$ with a pWW endpoint.

©2018 American Geophysical Union. All rights reserved.

Accepted Article

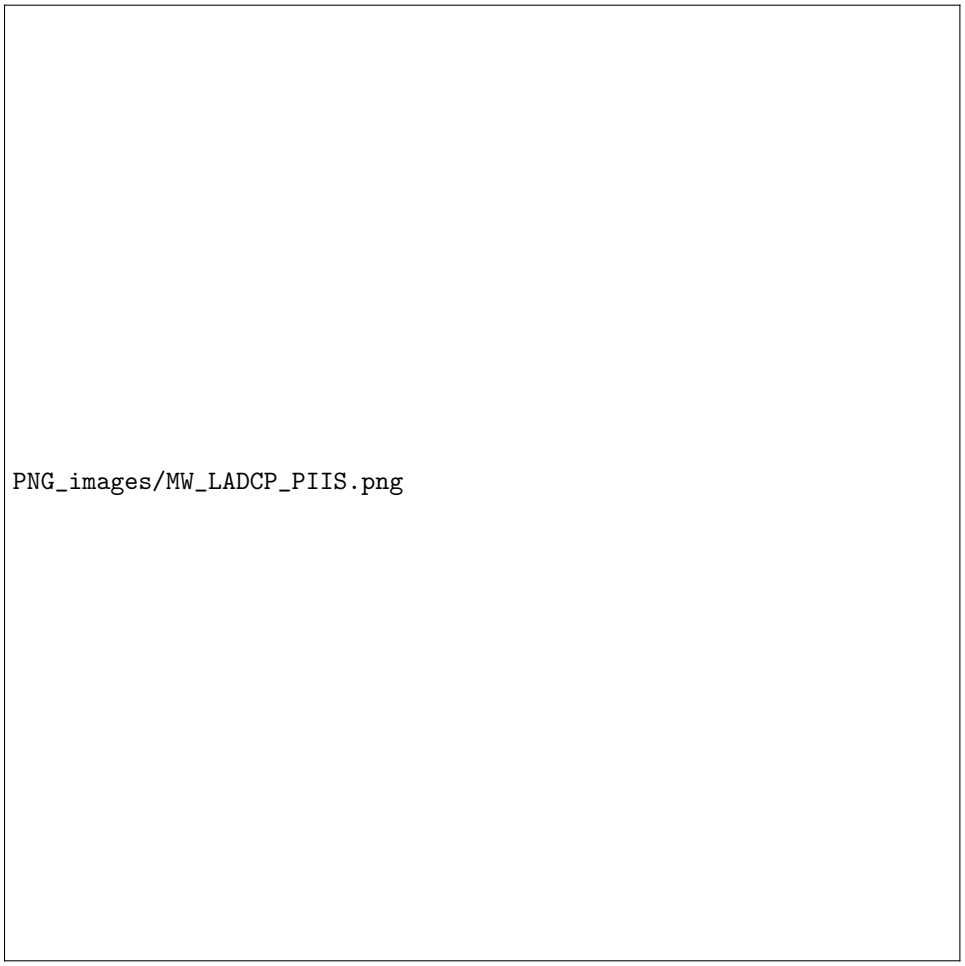

Figure 8. Figures showing GMW content (g kg^{-1}) and along channel velocities (m s^{-1}) for sections D (panels a,b) and C (panels c,d) as located in Figure 1. (a) and (c) Background color is GMW content from hydrographic tracers, colored dots show the GMW content from NG tracers. CTD stations are marked as black dashed lines, and above relevant stations the column inventories of SIM content (red) and MWI content (blue) are shown in metres. (b) and (d) Along channel velocity from LADCP measurements, positive values are off-shelf.

©2018 American Geophysical Union. All rights reserved.

Accepted Article

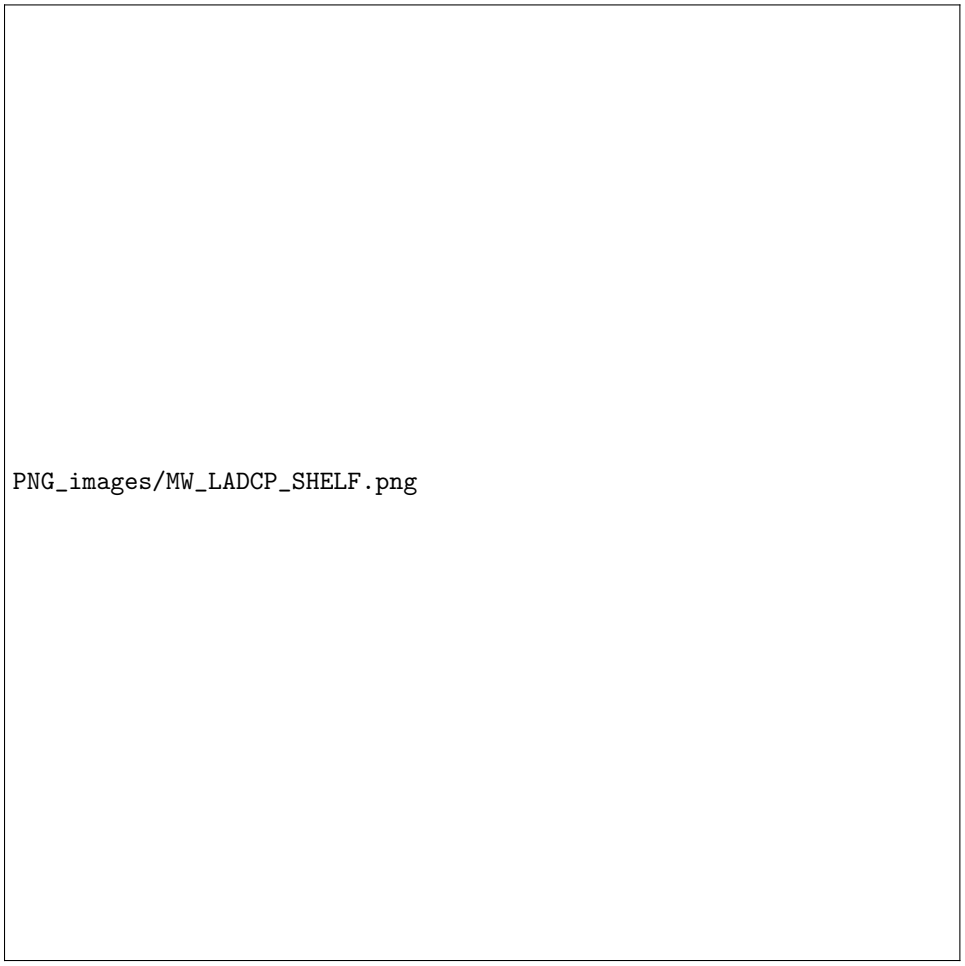

Figure 9. Figures showing GMW content (g kg^{-1}) and along channel velocities (m s^{-1}) for sections A (panels a,b) and B (panels c,d)as located in Figure 1. (a) and (c) Background color is GMW content from hydrographic tracers, colored dots show the GMW content from NG tracers. CTD stations are marked as black dashed lines, and above relevant stations the column inventories of SIM content (red) and MWI content (blue) are shown in metres. A false GMW is shaded in grey in panel d. (b) and (d) Along channel velocity from LADCP measurements, positive values are off-shelf.

©2018 American Geophysical Union. All rights reserved.

Figure 1.

Accepted Article

©2018 American Geophysical Union. All rights reserved.

Accepted Article

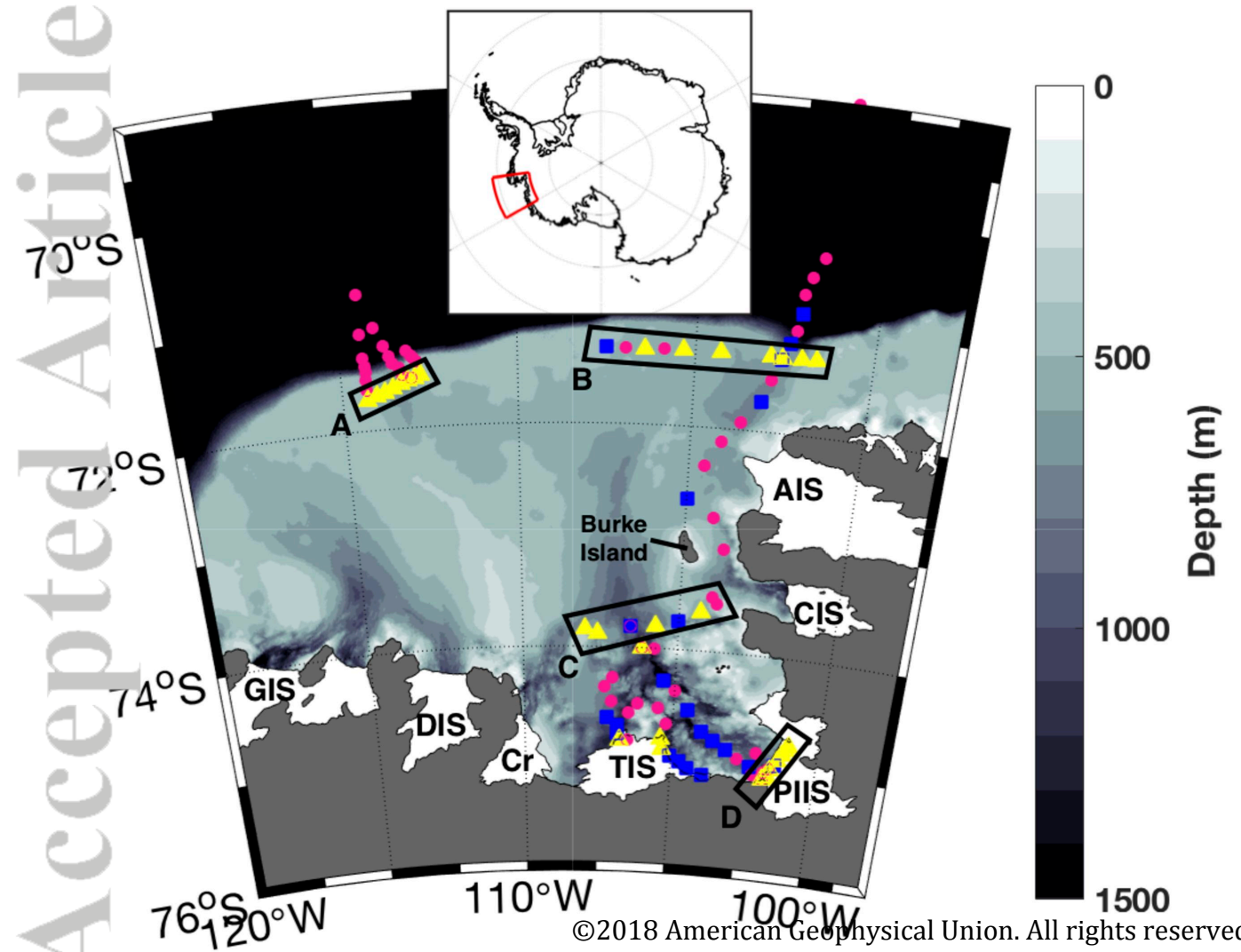

©2018 American Geophysical Union. All rights reserved

Figure 2.

Accepted Article

©2018 American Geophysical Union. All rights reserved.

Accepted Article

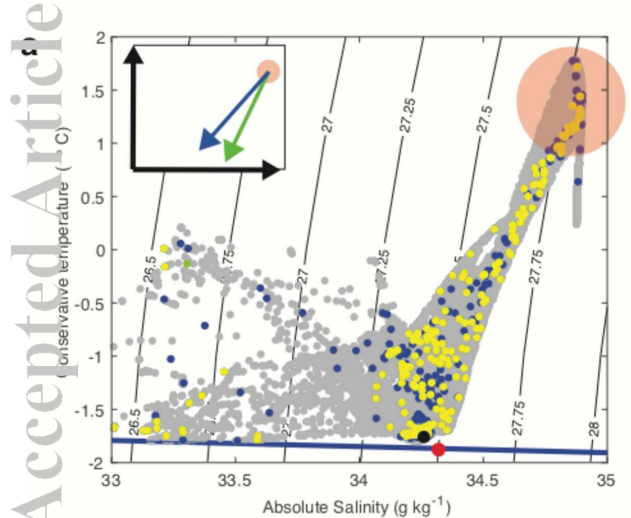

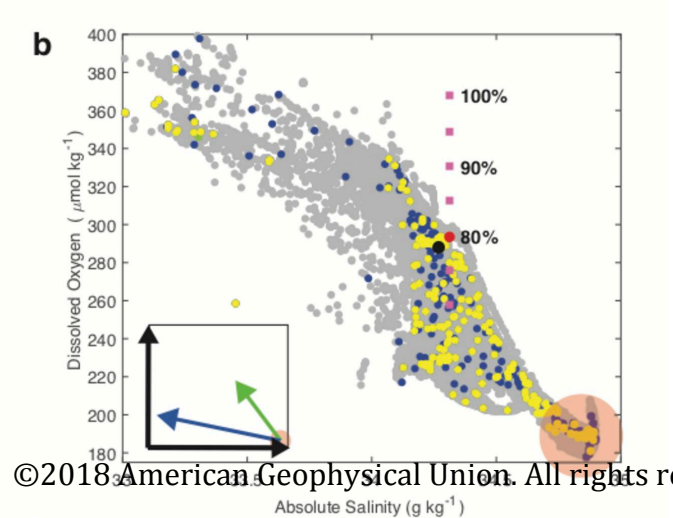

©2018 American Geophysical Union. All rights re

Figure 3.

Accepted Article

©2018 American Geophysical Union. All rights reserved.

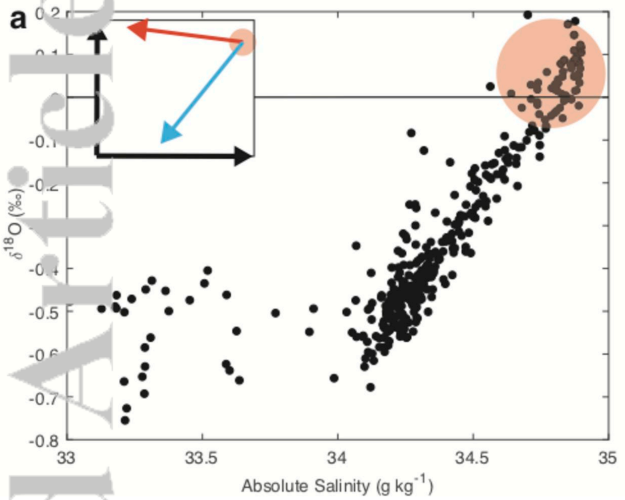

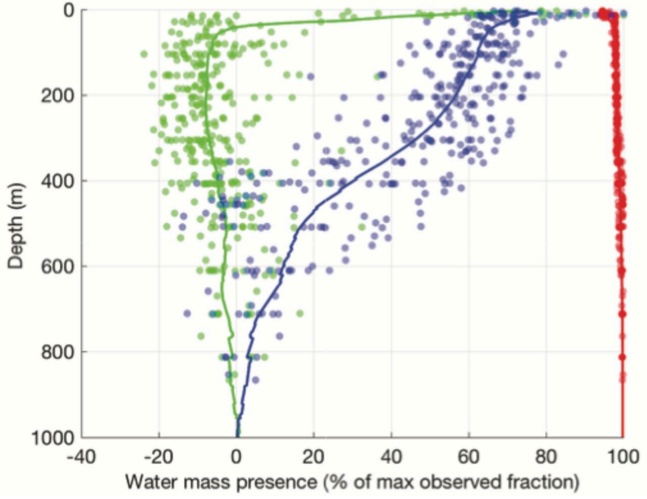

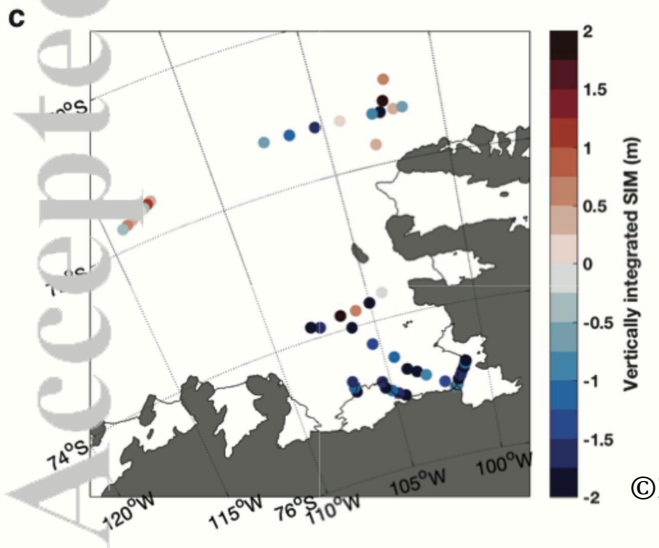

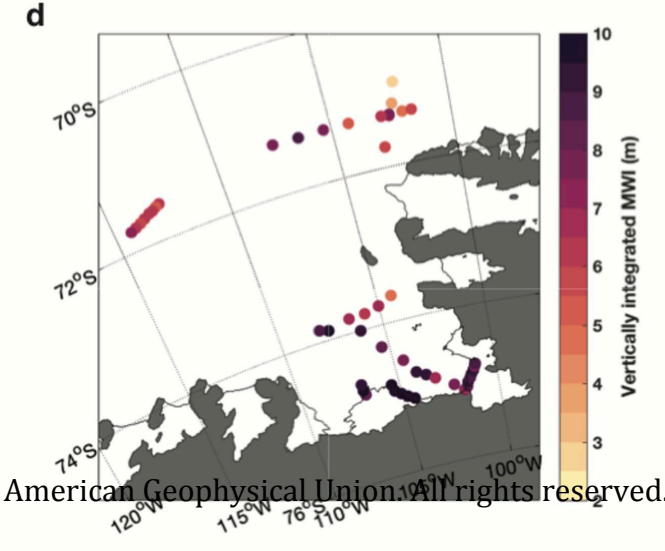

Accepted Article

©2018 American Geophysical Union. All rights reserved.

Figure 4.

Accepted Article

©2018 American Geophysical Union. All rights reserved.

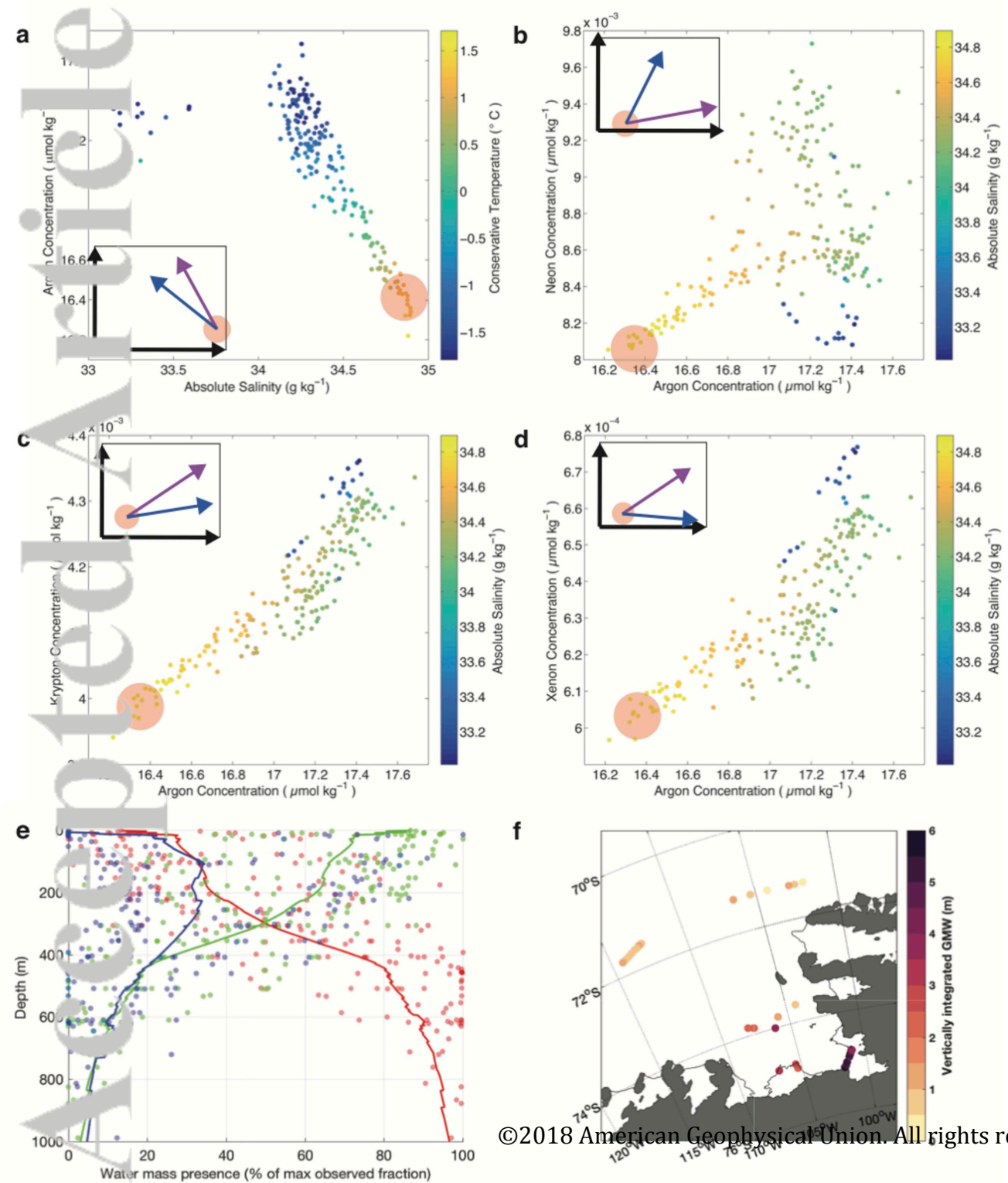

©2018 American Geophysical Union. All rights re

Figure 5.

Accepted Article

©2018 American Geophysical Union. All rights reserved.

Accepted Article

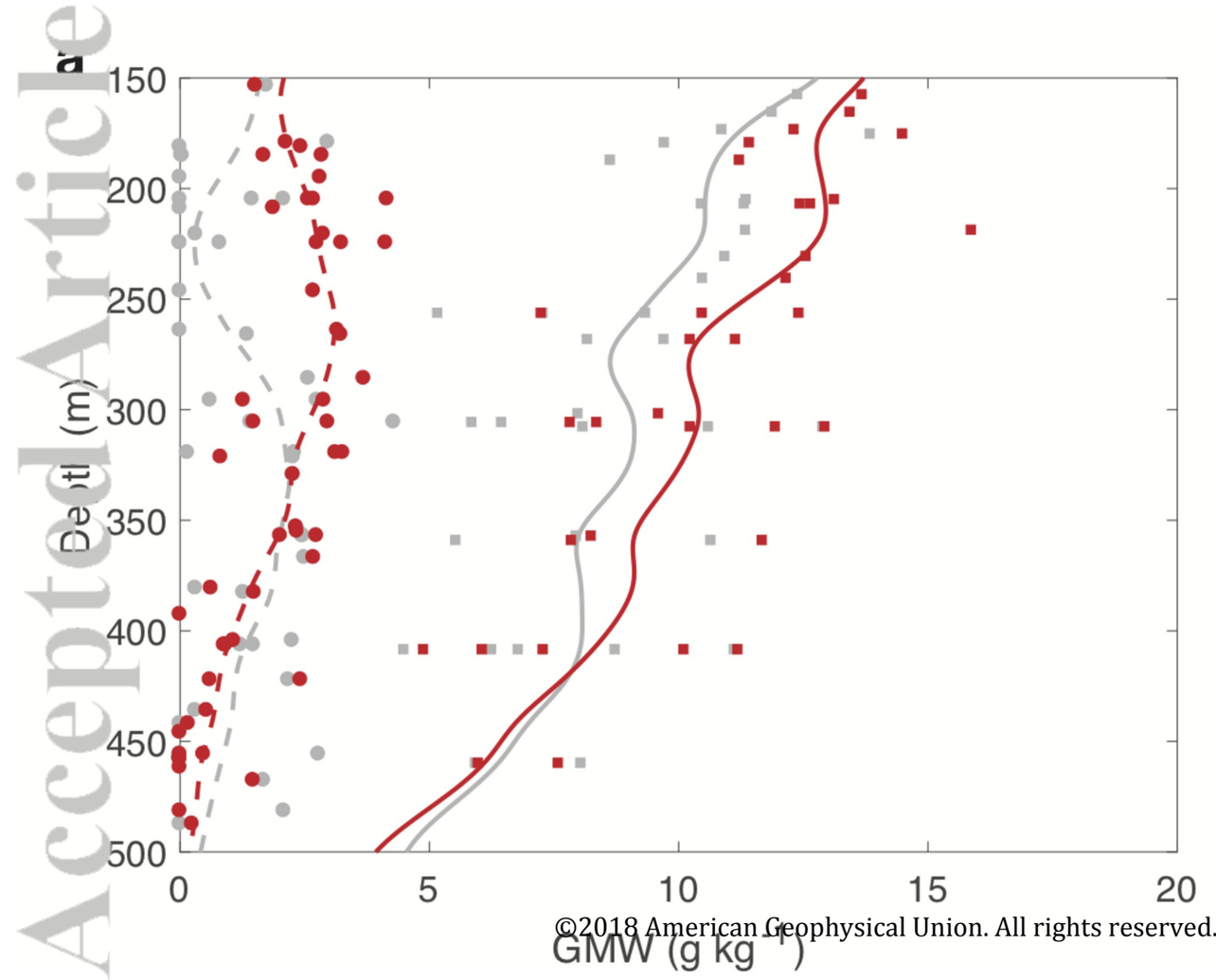

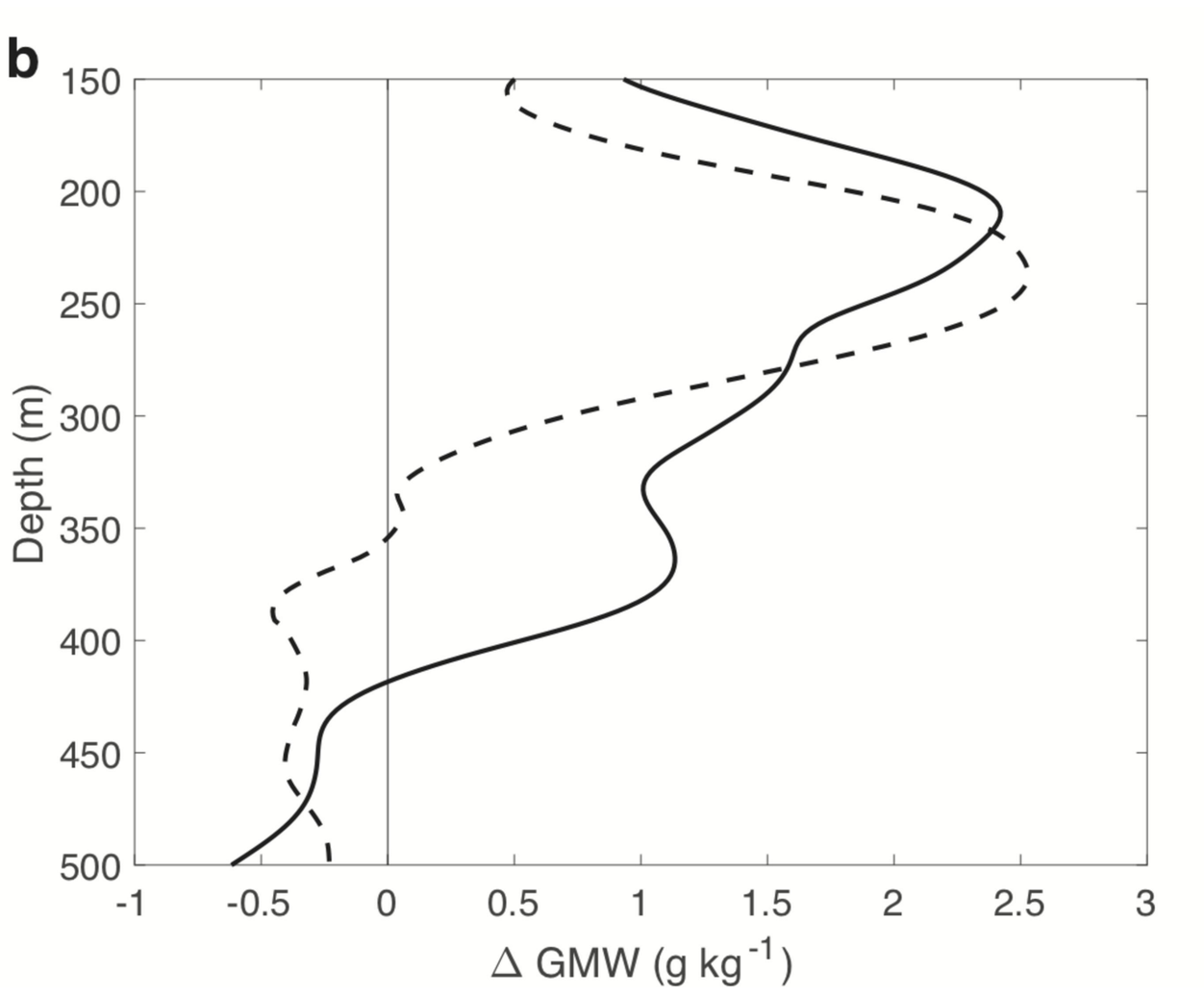

©2018 American Geophysical Union. All rights reserved.

Figure 6.

Accepted Article

©2018 American Geophysical Union. All rights reserved.

Accepted Article

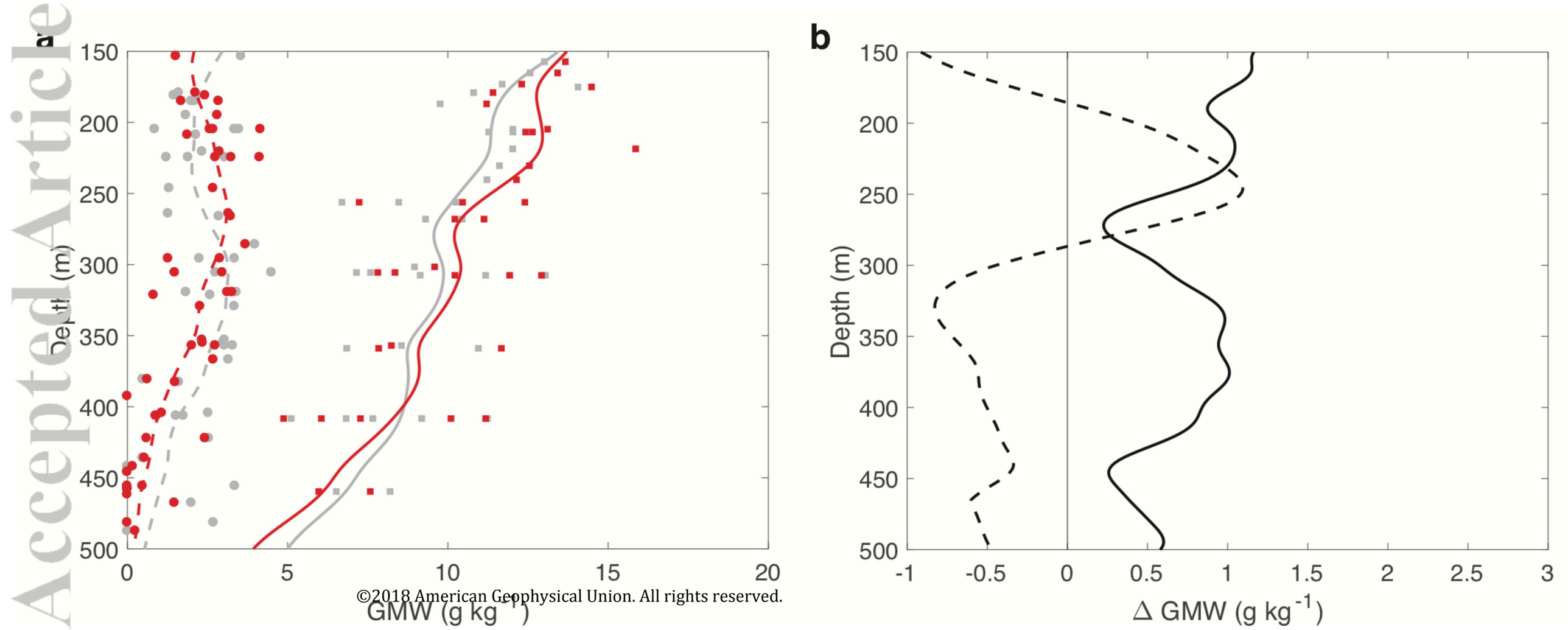

©2018 American Geophysical Union. All rights reserved.

Figure 7.

Accepted Article

©2018 American Geophysical Union. All rights reserved.

Accepted Article

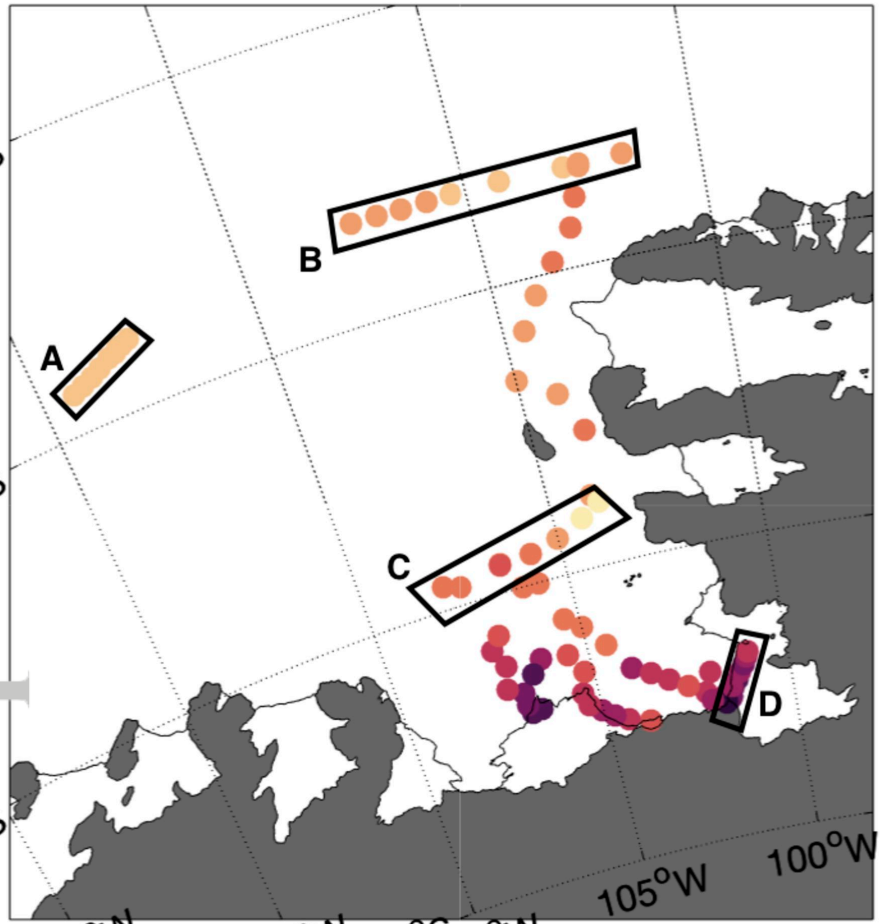

©2018 American Geophysical Union. All rig

Figure 8.

Accepted Article

©2018 American Geophysical Union. All rights reserved.

Accepted Article

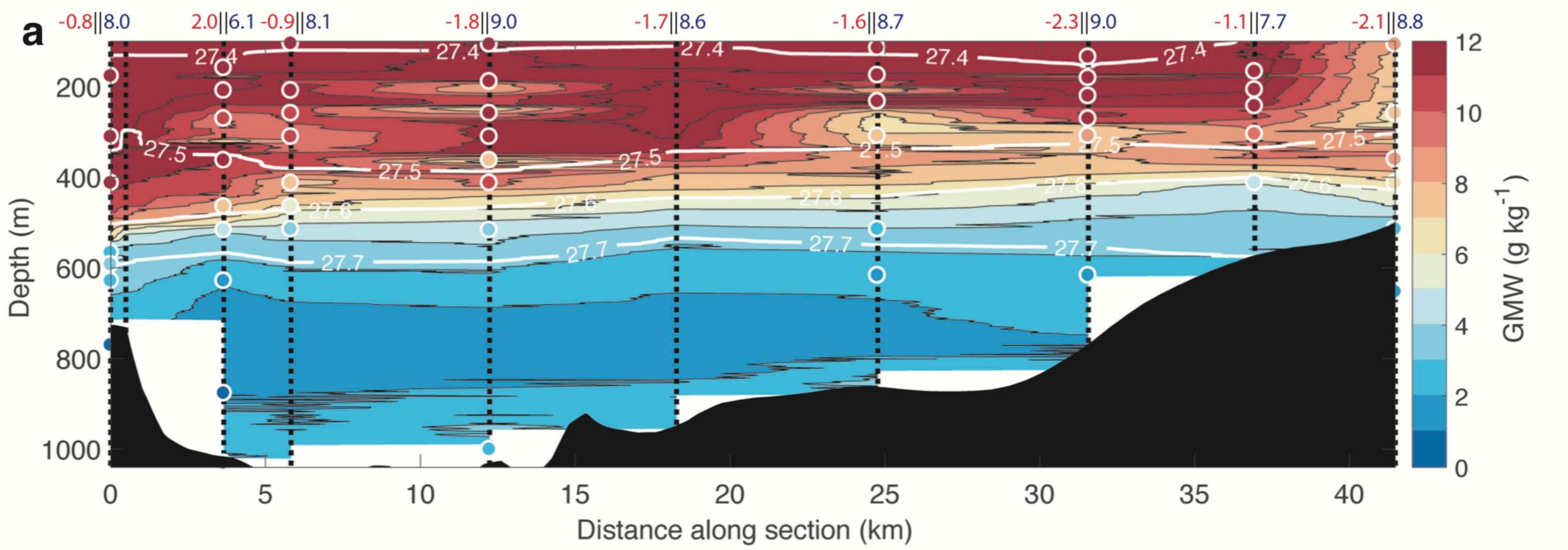

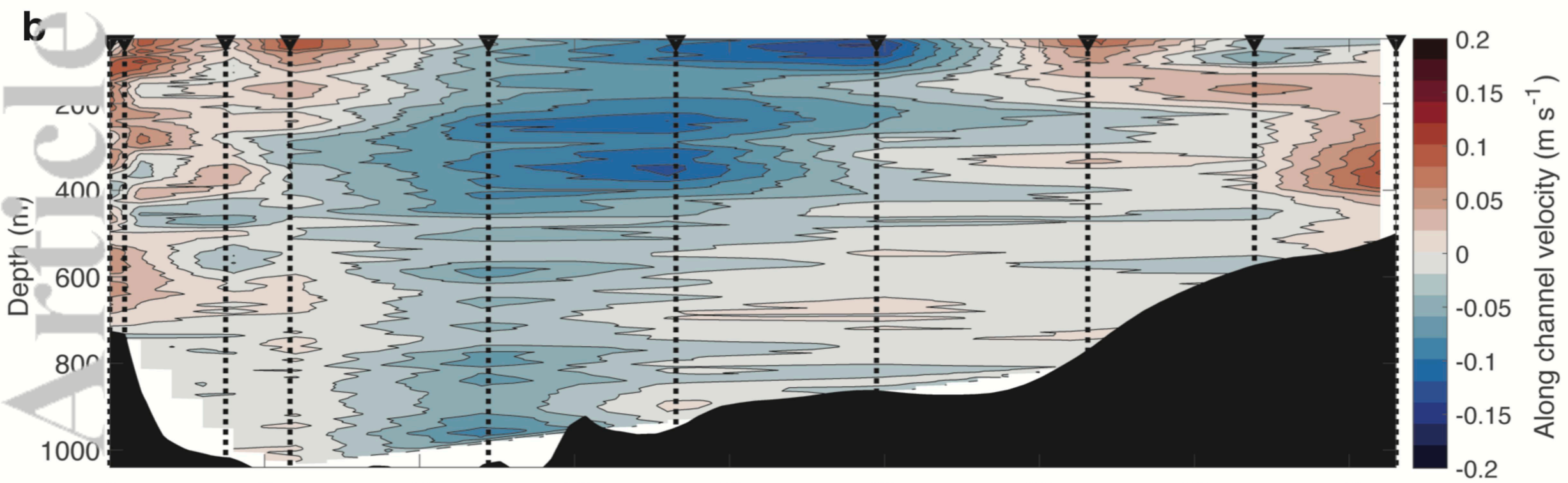

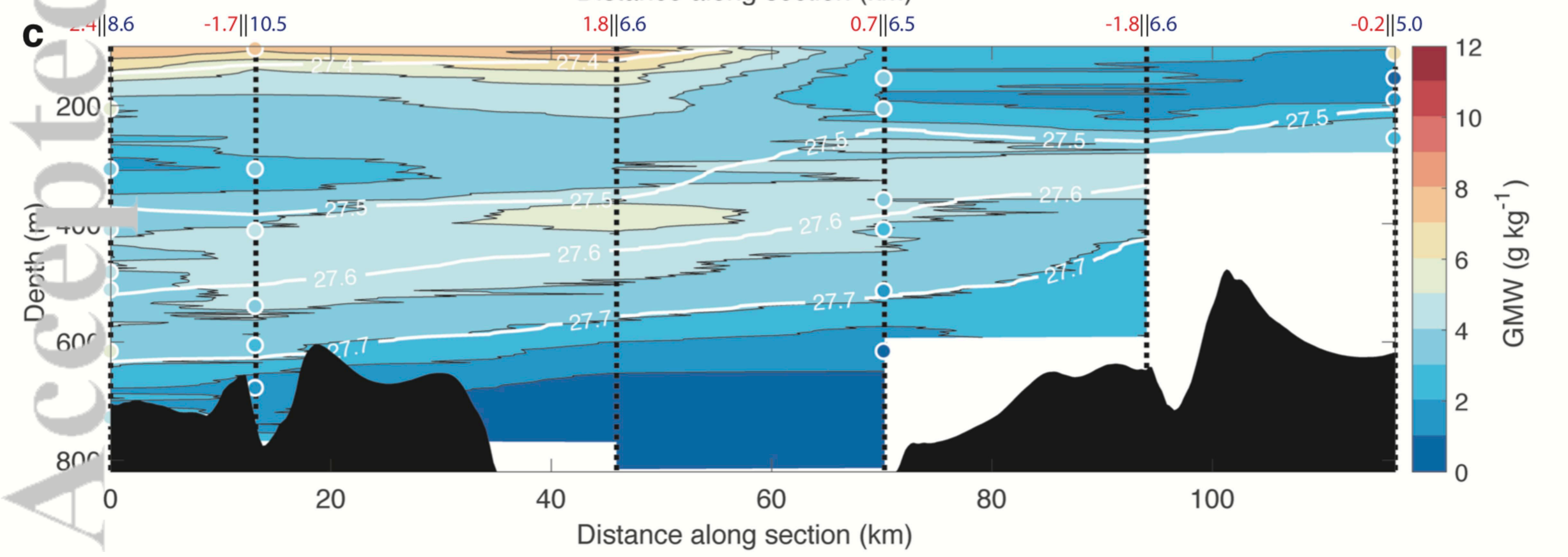

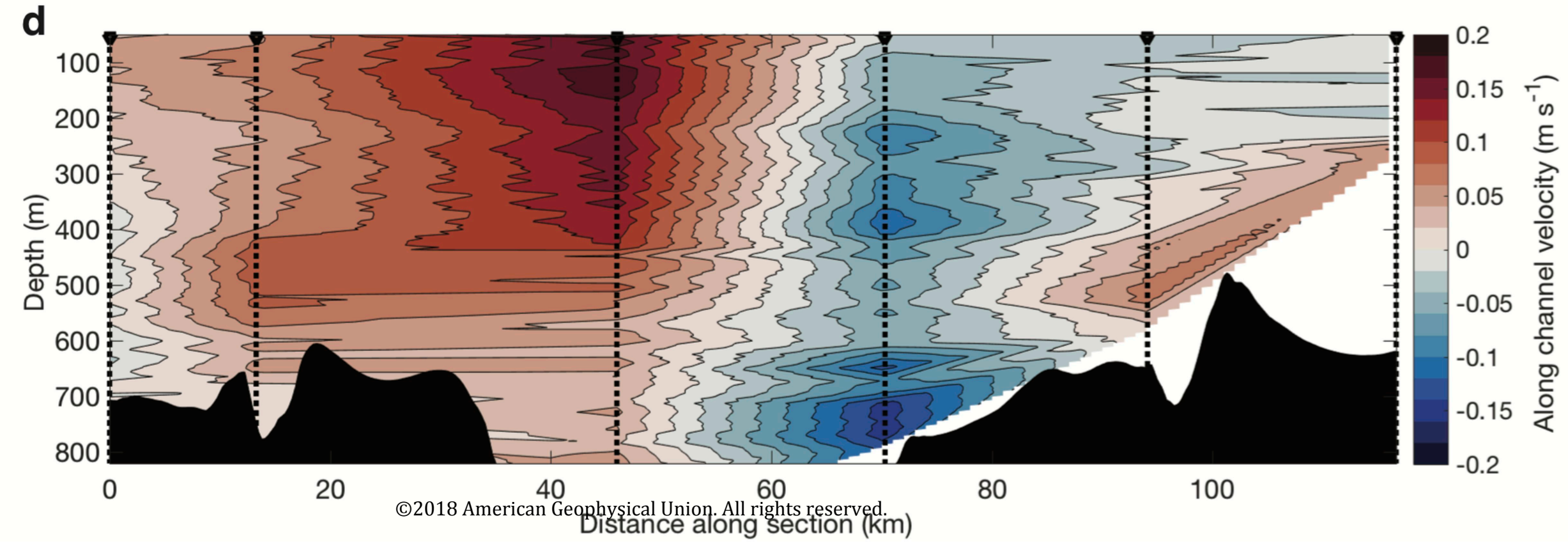

©2018 American Geophysical Union. All rights reserved.

Figure 9.

Accepted Article

©2018 American Geophysical Union. All rights reserved.

Accepted Article

©2018 American Geophysical Union. All rights reserved.

Accepted Article

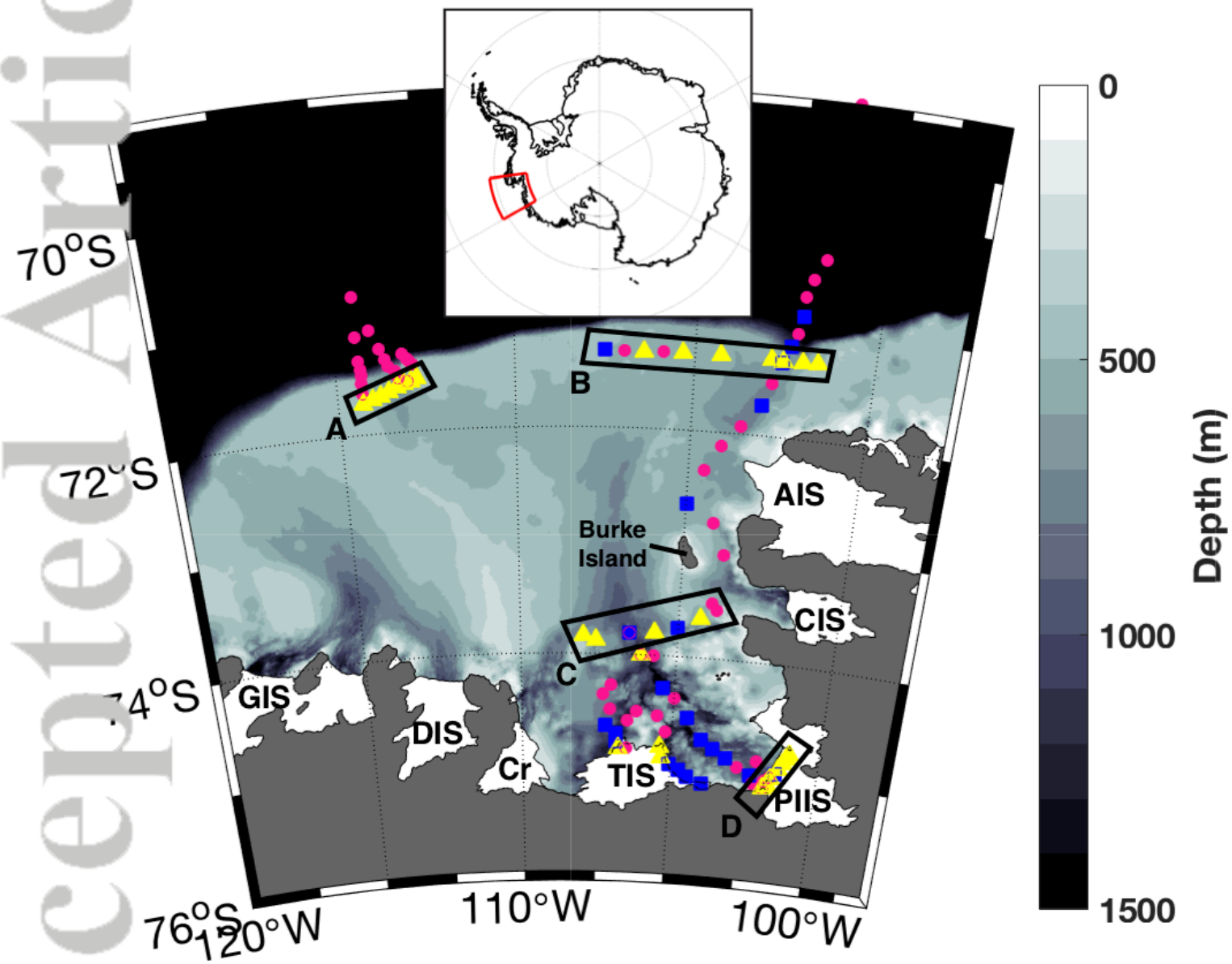

2019JC015133-f01-z-.png

©2018 American Geophysical Union. All rights reserved.

Accepted Article

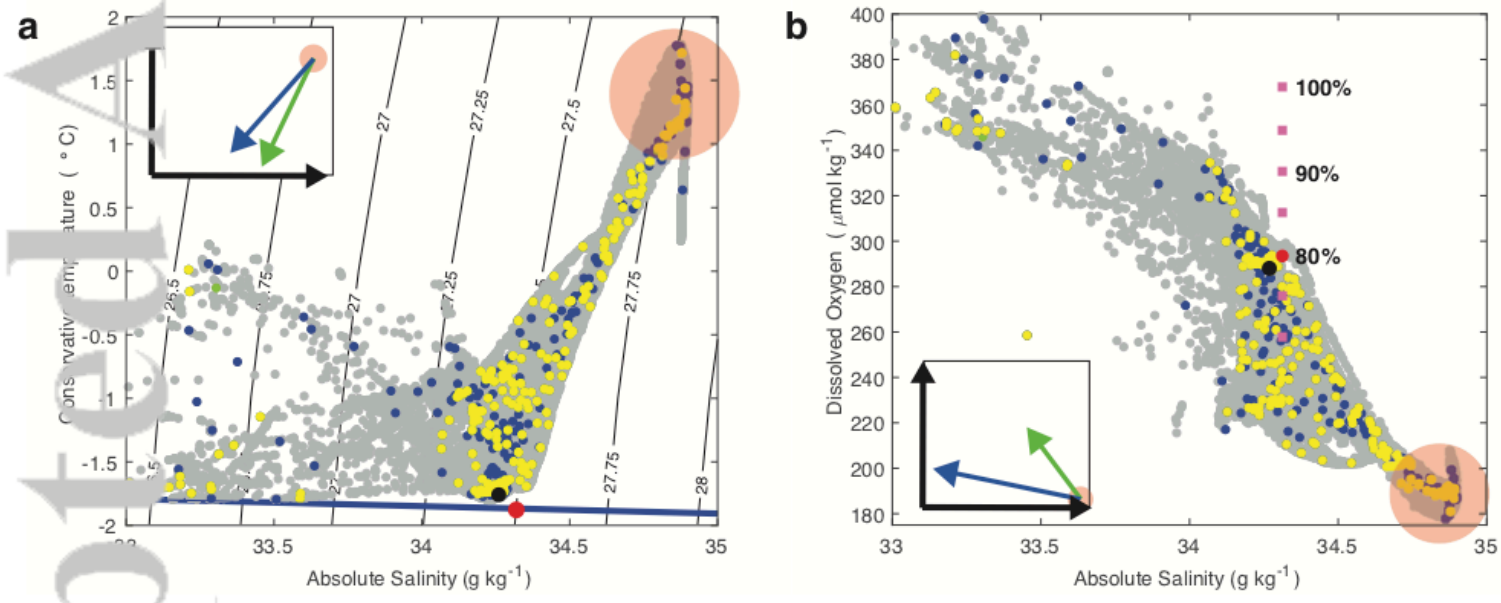

2019JC015133-f02-z-.png

©2018 American Geophysical Union. All rights reserved.

Accepted Article

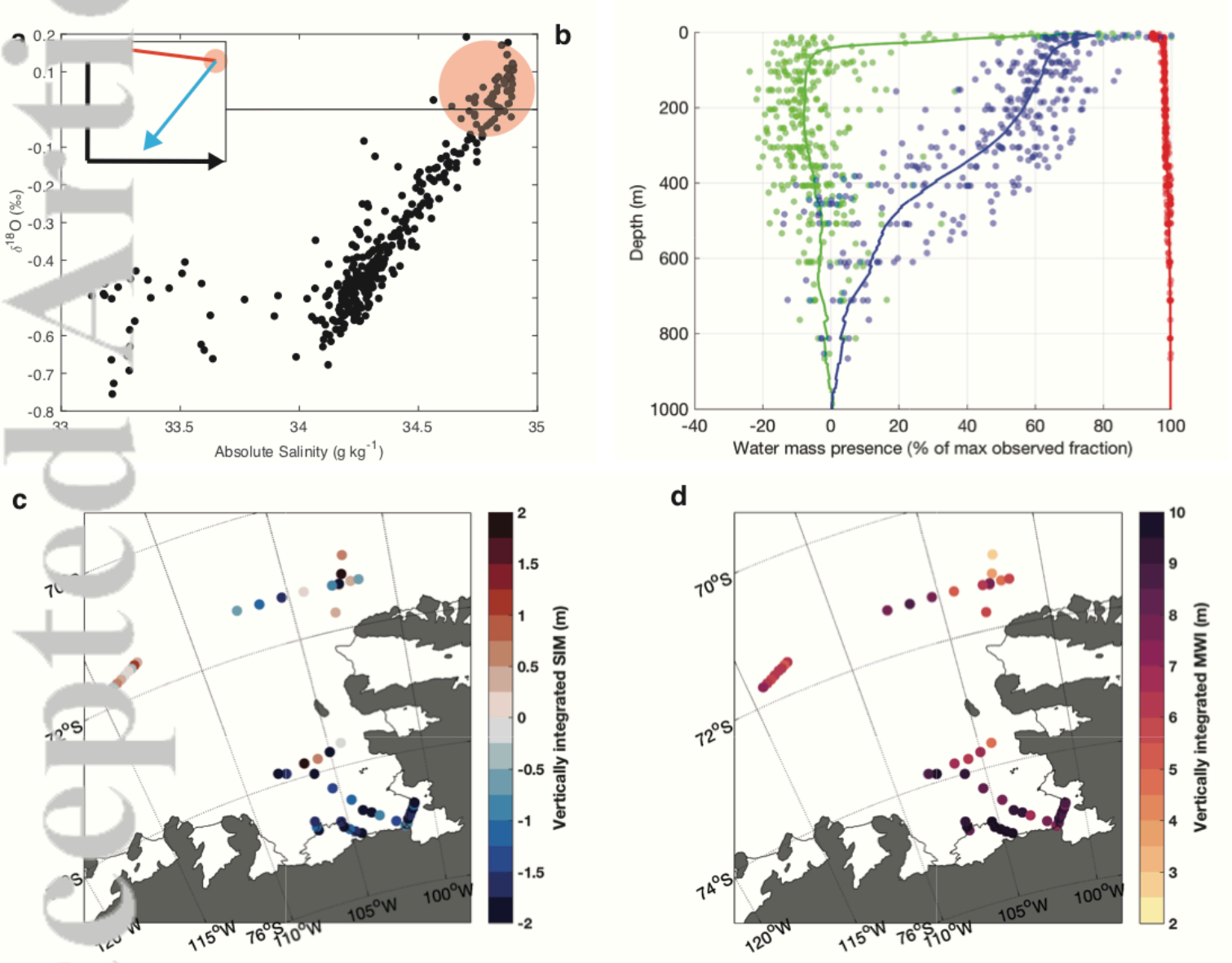

2019JC015133-f03-z-.png

©2018 American Geophysical Union. All rights reserved.

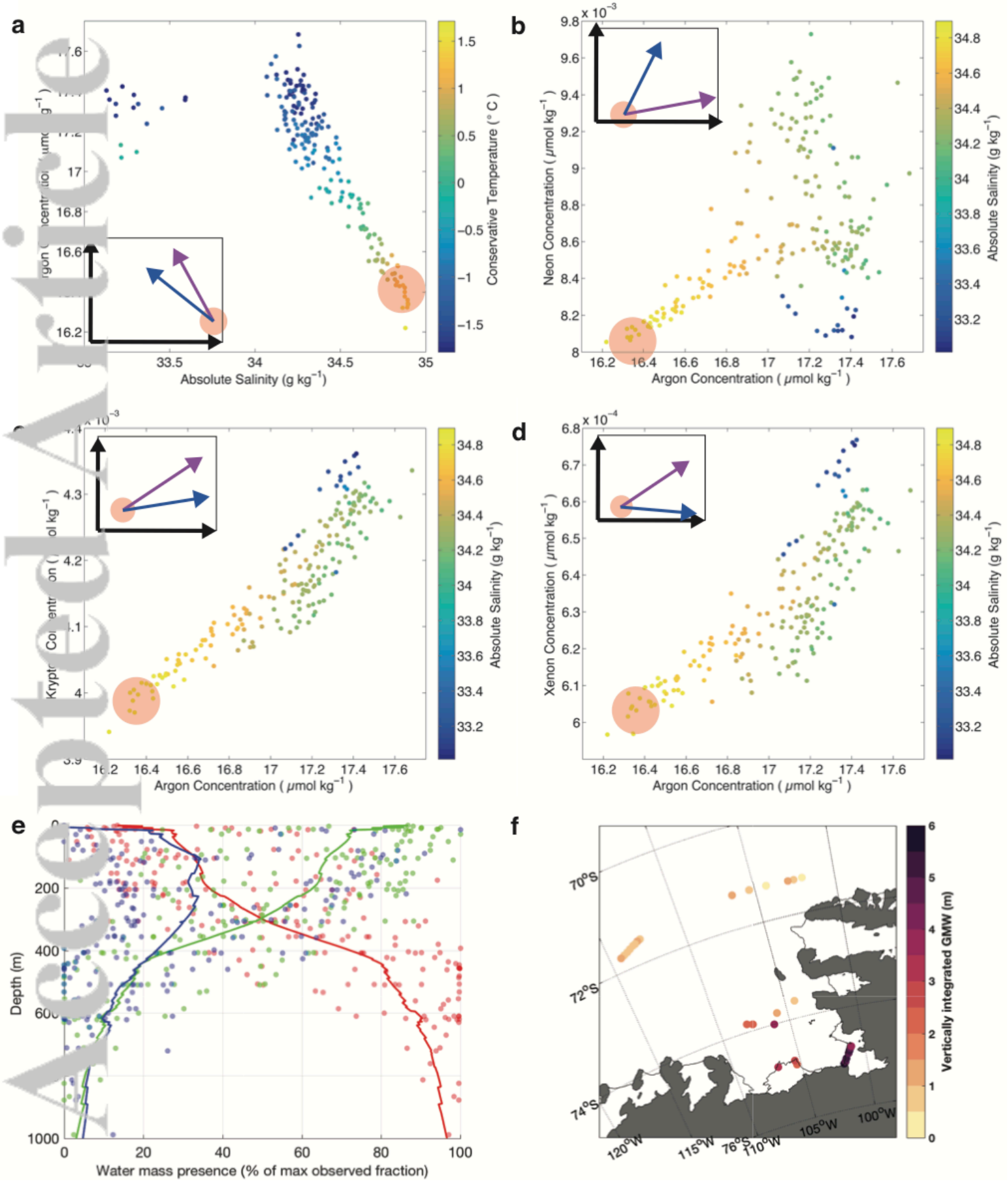

2019JC015133-f04-z-.png

©2018 American Geophysical Union. All rights reserved.

Accepted Article

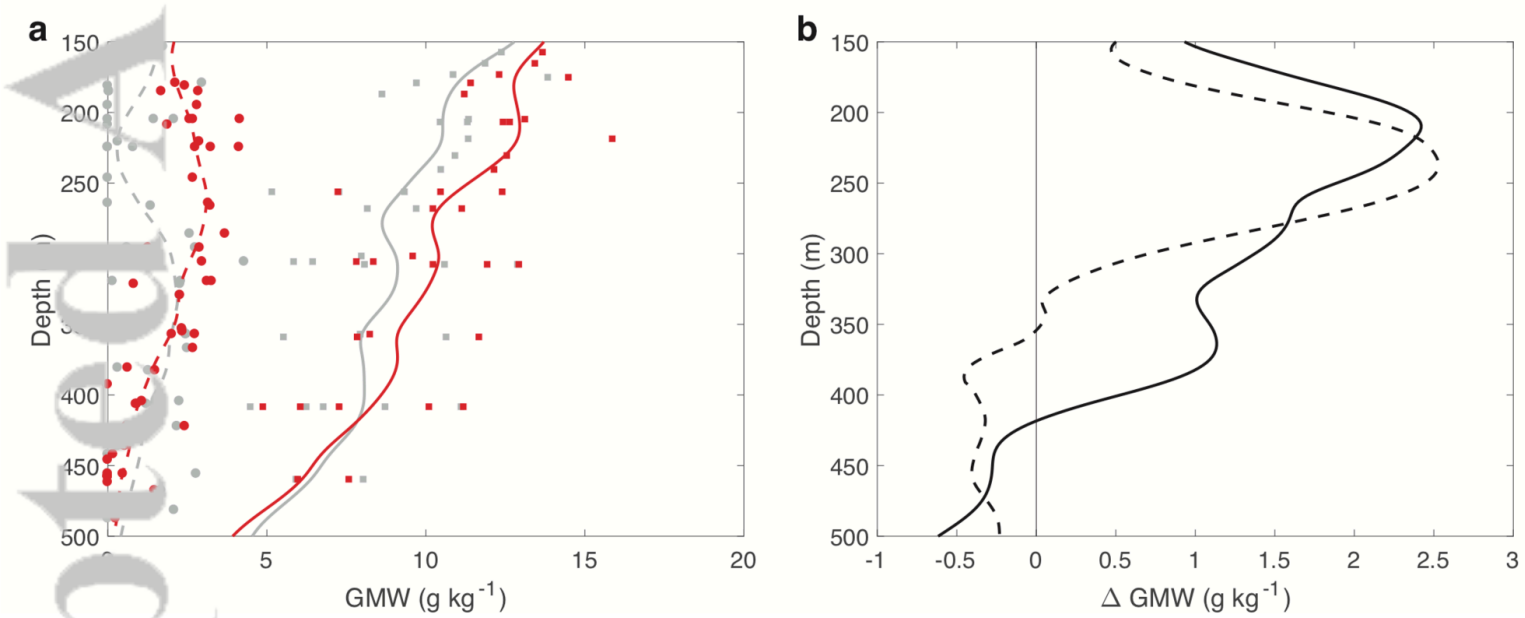

2019JC015133-f05-z-.png

©2018 American Geophysical Union. All rights reserved.

Accepted Article

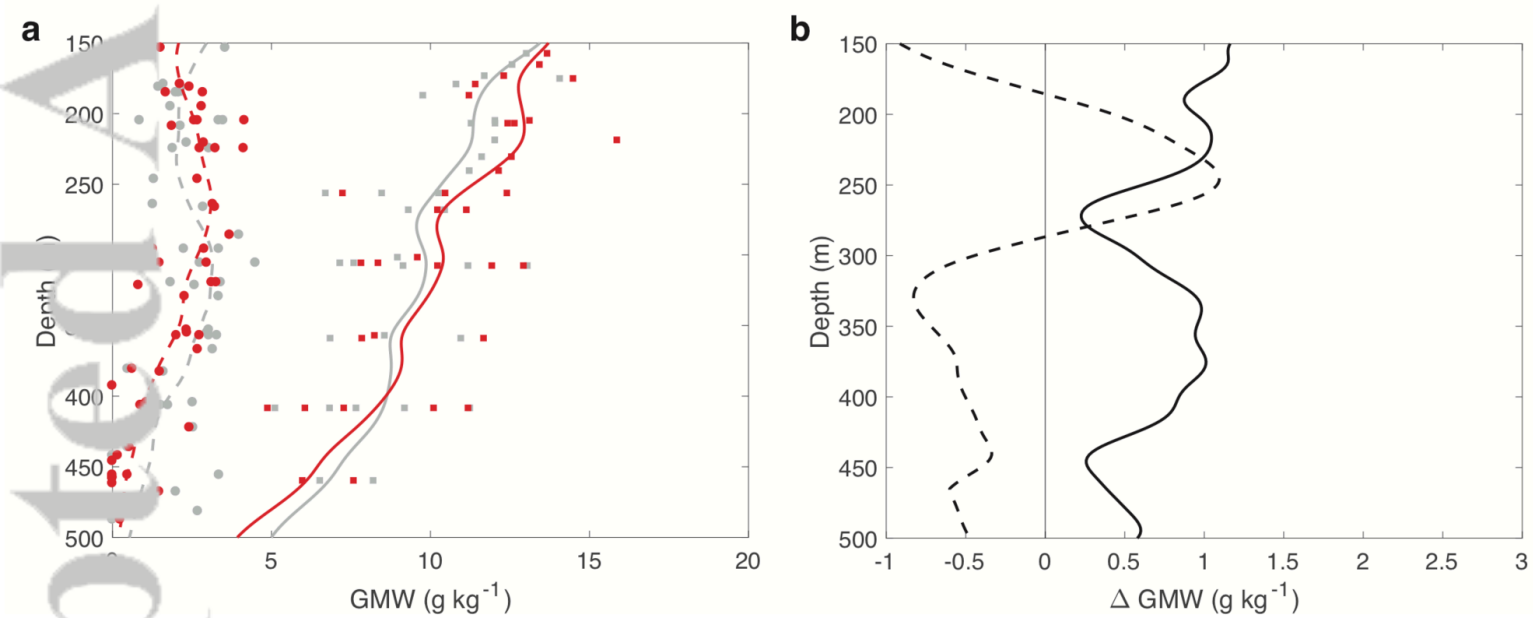

2019JC015133-f06-z-.png

©2018 American Geophysical Union. All rights reserved.

Accepted Article

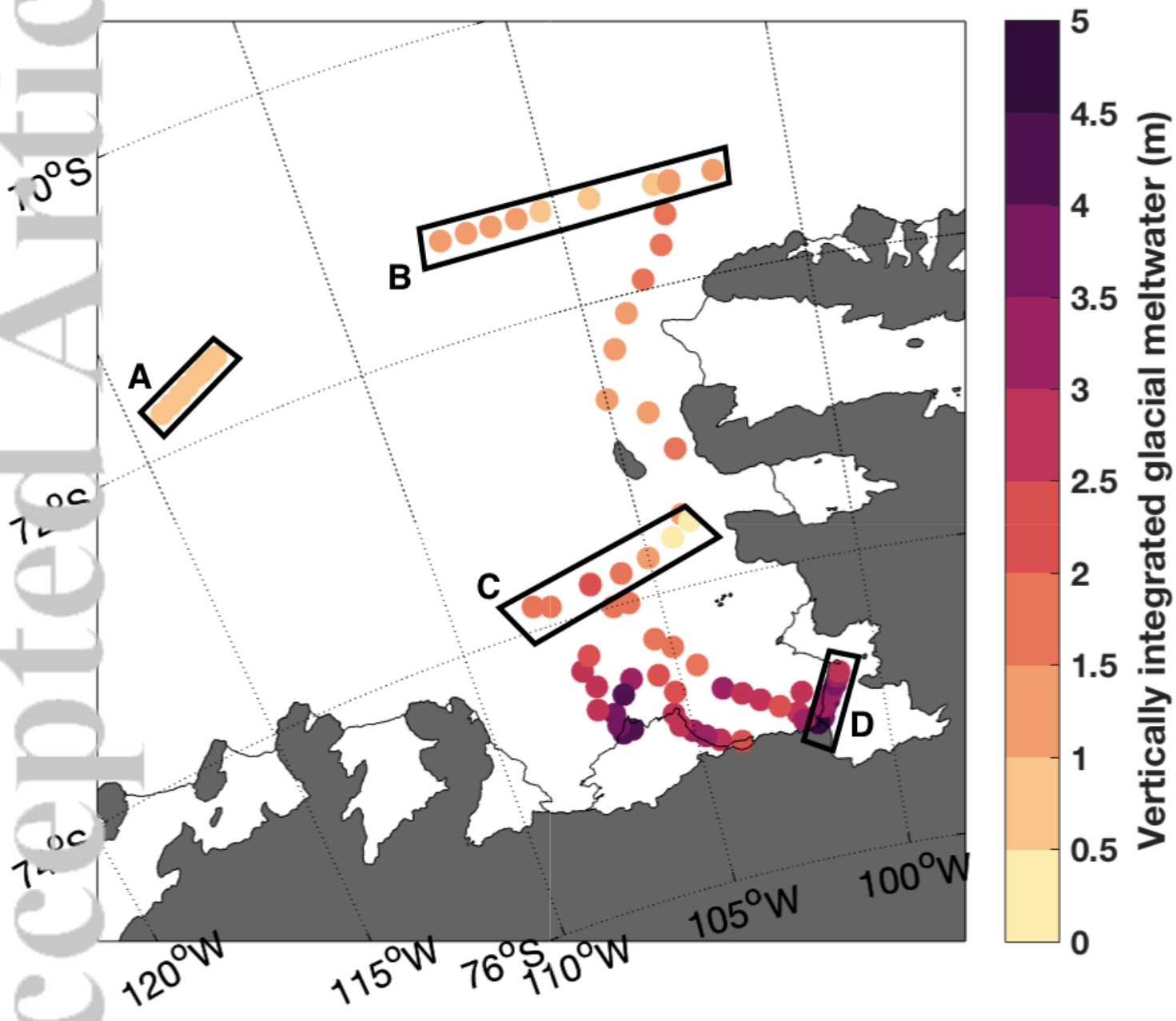

2019JC015133-f07-z-.png

©2018 American Geophysical Union. All rights reserved.

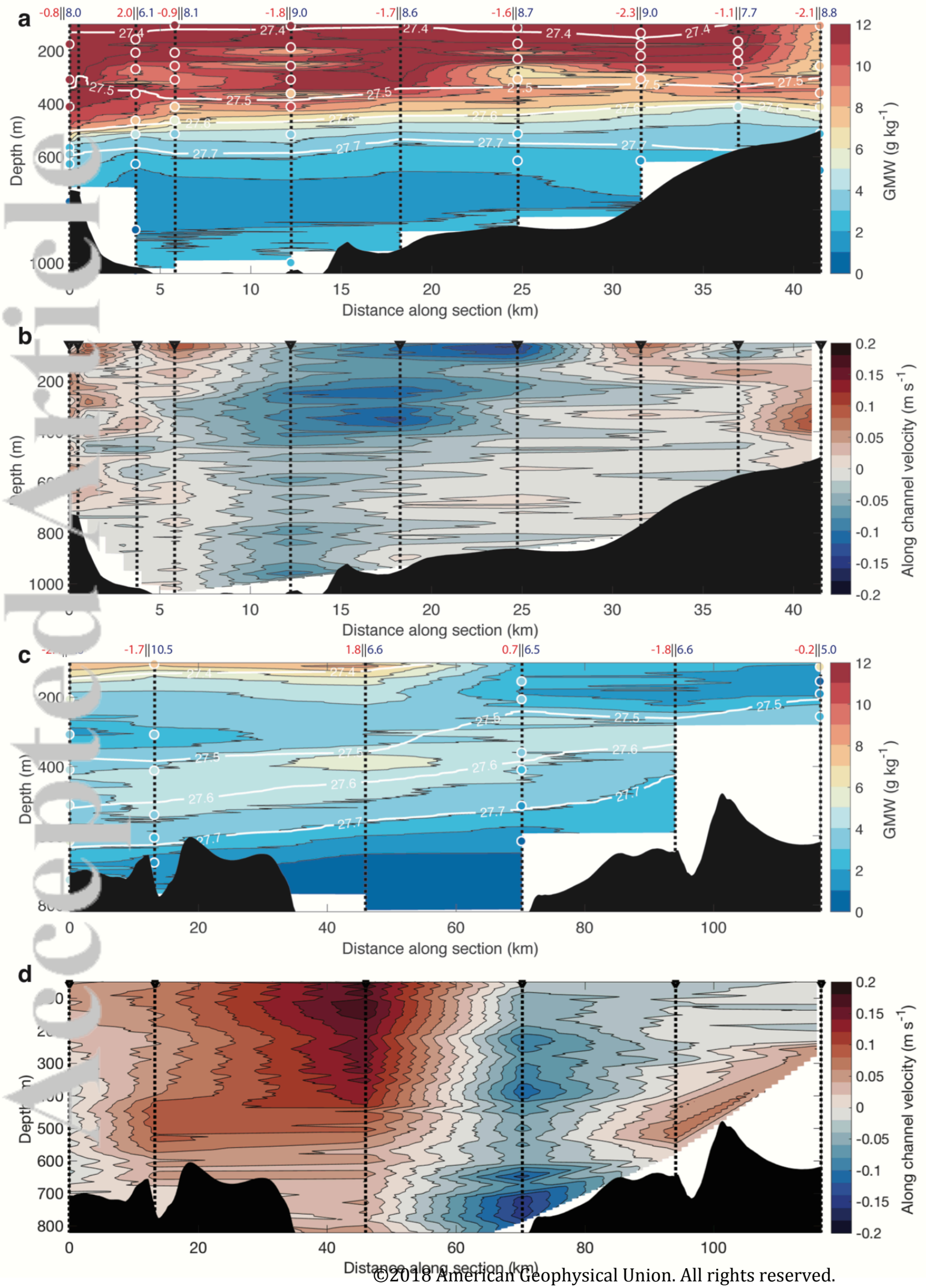

©2018 American Geophysical Union. All rights reserved.
2019JC015133-f08-z-.png

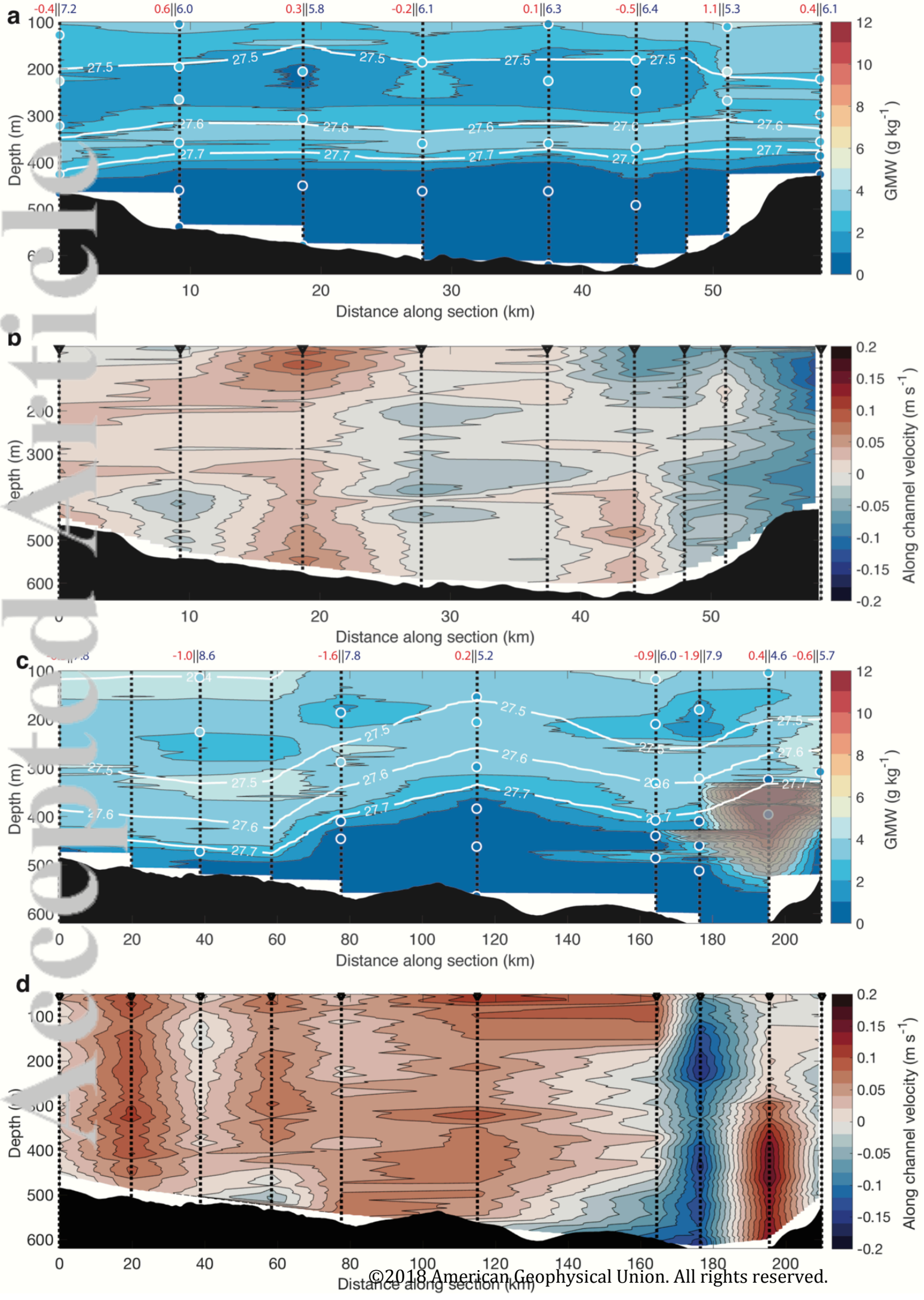

©2018 American Geophysical Union. All rights reserved.